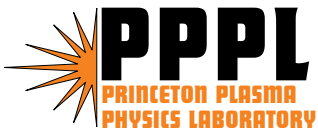


**Internal Kink Mode Dynamics  
in High-beta NSTX Plasmas**

J.E. Menard, R.E. Bell, E.D. Fredrickson, D.A. Gates,  
S.M. Kaye, B.P. LeBlanc, S.S. Medley, W. Park,  
S.A. Sabbagh, A. Sontag, D. Stutman, K. Tritz,  
W. Zhu and the NSTX Research Team

December 2004



# PPPL Report Disclaimers

## Full Legal Disclaimer

This report was prepared as an account of work sponsored by an agency of the United States Government. Neither the United States Government nor any agency thereof, nor any of their employees, nor any of their contractors, subcontractors or their employees, makes any warranty, express or implied, or assumes any legal liability or responsibility for the accuracy, completeness, or any third party's use or the results of such use of any information, apparatus, product, or process disclosed, or represents that its use would not infringe privately owned rights. Reference herein to any specific commercial product, process, or service by trade name, trademark, manufacturer, or otherwise, does not necessarily constitute or imply its endorsement, recommendation, or favoring by the United States Government or any agency thereof or its contractors or subcontractors. The views and opinions of authors expressed herein do not necessarily state or reflect those of the United States Government or any agency thereof.

## Trademark Disclaimer

Reference herein to any specific commercial product, process, or service by trade name, trademark, manufacturer, or otherwise, does not necessarily constitute or imply its endorsement, recommendation, or favoring by the United States Government or any agency thereof or its contractors or subcontractors.

# PPPL Report Availability

This report is posted on the U.S. Department of Energy's Princeton Plasma Physics Laboratory Publications and Reports web site in Fiscal Year 2005. The home page for PPPL Reports and Publications is: [http://www.pppl.gov/pub\\_report/](http://www.pppl.gov/pub_report/)

## Office of Scientific and Technical Information (OSTI):

Available electronically at: <http://www.osti.gov/bridge>.

Available for a processing fee to U.S. Department of Energy and its contractors, in paper from:

U.S. Department of Energy  
Office of Scientific and Technical Information  
P.O. Box 62  
Oak Ridge, TN 37831-0062  
Telephone: (865) 576-8401  
Fax: (865) 576-5728  
E-mail: [reports@adonis.osti.gov](mailto:reports@adonis.osti.gov)

## National Technical Information Service (NTIS):

This report is available for sale to the general public from:

U.S. Department of Commerce  
National Technical Information Service  
5285 Port Royal Road  
Springfield, VA 22161  
Telephone: (800) 553-6847  
Fax: (703) 605-6900  
Email: [orders@ntis.fedworld.gov](mailto:orders@ntis.fedworld.gov)  
Online ordering: <http://www.ntis.gov/ordering.htm>

# Internal kink mode dynamics in high-beta NSTX plasmas

J.E. Menard<sup>1</sup>, R.E. Bell<sup>1</sup>, E.D. Fredrickson<sup>1</sup>, D.A. Gates<sup>1</sup>,  
S.M. Kaye<sup>1</sup>, B.P. LeBlanc<sup>1</sup>, S.S. Medley<sup>1</sup>, W. Park<sup>1</sup>,  
S.A. Sabbagh<sup>2</sup>, A. Sontag<sup>2</sup>, D. Stutman<sup>3</sup>, K. Tritz<sup>3</sup>, W. Zhu<sup>2</sup>  
and the NSTX Research Team.

<sup>1</sup>Princeton Plasma Physics Laboratory, Princeton, NJ, USA

<sup>2</sup>Columbia University, New York, NY, USA

<sup>3</sup>Johns Hopkins University, Baltimore, MD, USA

## **Abstract.**

Saturated internal kink modes have been observed in many of the highest toroidal  $\beta$  discharges of the National Spherical Torus Experiment (NSTX). These modes often cause rotation flattening in the plasma core, can degrade energy confinement, and in some cases contribute to the complete loss of plasma angular momentum and stored energy. Characteristics of the modes are measured using soft X-ray, kinetic profile, and magnetic diagnostics. Toroidal flows approaching Alfvénic speeds, island pressure peaking, and enhanced viscous and diamagnetic effects associated with high- $\beta$  may contribute to mode non-linear stabilization. These saturation mechanisms are investigated for NSTX parameters and compared to experimental data.

PACS numbers: 52.55.Fa, 52.55.Tn, 52.35.Py

## 1. Introduction

The Spherical Torus (ST) [1] configuration is presently being actively investigated as a potentially high- $\beta$  and compact magnetic confinement concept. The National Spherical Torus Experiment (NSTX) [2] and the Mega-Ampere Spherical Tokamak (MAST) [3] are presently the largest ST devices in the world fusion program. These devices have achieved both high confinement [4, 5] and high  $\beta$ . NSTX has achieved both high toroidal- $\beta$ ,  $\beta_T \equiv 2\mu_0\langle p \rangle / B_{T0}^2$  up to 35%, and high normalized- $\beta$ ,  $\beta_N \equiv \beta_T a B_{T0} / I_P$  up to 6.5% mT/MA [6, 7] using up to 7MW of deuterium Neutral Beam Injection (NBI) heating.

In the highest  $\beta_T$  discharges, obtained at high  $I_P / a B_{T0} > 6\text{MA/mT}$ , the central safety factor inferred from EFIT reconstructions [8, 9, 10] based on external magnetic measurements, simulations of resistive current diffusion, and preliminary Motional Stark Effect (MSE) data [11], is typically near 1 with a wide region of low magnetic shear. Such discharges are computed to be ideally unstable to  $n=1$  pressure-driven internal kink instabilities, and experimentally the onset of  $n=1$  activity is often observed near the computed instability thresholds. While operating regimes with high- $l_i$  and low to moderate beta exist in NSTX where sawteeth are routinely observed, at high  $\beta$ , sawteeth are relatively rare, and it is more common for a core 1/1 mode to grow slowly and saturate in amplitude even for  $\beta$  values well above the computed ideal (no-wall) limit at mode onset. In this manuscript we explore possible saturation mechanisms for the 1/1 mode in NSTX, and attempt to compare the available experimental data to various stabilization theories. While the ultimate aim of NSTX research is to avoid the 1/1 mode by operating with elevated  $q$ , until fully non-inductive current drive scenarios are developed, eventually current diffusion will cause the  $q=1$  to enter the plasma. Further, the high  $\beta$  and near-Alfvénic toroidal flow speeds achievable in NSTX plasmas could significantly alter the behavior of the 1/1 instability. Thus, the ST offers

a potentially unique configuration to better understand the underlying physics that controls the sawtooth instability.

The remainder of this article is outlined as follows. First, Section 2 discusses the impact of the 1/1 mode on fast-ion and thermal confinement, the impact of the mode on the plasma toroidal rotation, and the possible role of rapid rotation on the mode stability. Methods for estimating the island mode structure from Ultra-Soft X-ray (USXR) diagnostics are described, and the inferred mode fields are used to estimate rotation damping from neoclassical toroidal viscous damping theory. Several additional possible mode saturation mechanisms are discussed including the role of enhanced viscosity, pressure peaking inside the island, and non-linearly enhanced diamagnetic flows. These results are summarized in Section 3. Lastly, Section 4 describes in more detail how island-model-constrained USXR tomography has been used to follow 1/1 island dynamics during the growth and saturation phase of high beta discharges.

## 2. Experimental Results and Interpretation

In this section, experimental data is presented illustrating the behavior and effects of internal modes in NSTX high- $\beta$  discharges as evident in the stored energy, neutron rate, USXR, and magnetic fluctuation diagnostic data. In the present context, high- $\beta$  corresponds roughly to  $\beta_T > 25\%$  where  $\beta_T = 2\mu_0\langle p\rangle/B_{T0}^2$ ,  $\langle p\rangle$  is the volume-average pressure, and  $B_{T0}$  is the vacuum toroidal field at the plasma geometric center. For the case of the saturated 1/1 mode, the mode is obviously linearly unstable but non-linearly stable, or nearly so. A variety of possible stabilization and saturation mechanisms are described below and compared to the experimental data. These comparisons are often qualitative, as non-linear treatments of the internal mode stability are difficult both analytically and computationally. Further, systematic  $q$  profile measurements are not

yet available, so precise linear stability growth rate calculations are not yet feasible.

### 2.1. Fast particle effects

Fast ions are well known to excite a variety of MHD instabilities, and several types of fast-ion-induced modes have been observed on NSTX ranging in frequency from the Compressional Alfvén Eigenmode (CAE) [12, 13] ( $f=0.5\text{-}2\text{MHz}$ ) to the Toroidal Alfvén Eigenmode (TAE) ( $f=20\text{-}200\text{kHz}$ ) and “bounce” and bounce-precession fishbones [14] ( $f < 100\text{kHz}$ ). On the other hand, trapped energetic ions are also well known [15] to help stabilize the internal kink mode. In tokamaks, this stabilization can delay the occurrence of normal sawteeth, allow the current profile to penetrate on axis, and ultimately lead to monster sawteeth [16, 17] with large inversion radius. For reference, the low aspect ratio of NSTX makes the trapped particle fraction (for zero banana width) at least 50% over nearly 90 typical plasmas. As stated previously, cyclic sawtooth activity is relatively rare in high  $\beta$  discharges in NSTX, and many of the highest  $\beta$  discharges are instead confinement limited by saturated  $m/n = 1/1$  modes as shown in Figure 1. This confinement degradation is evident in Figures 1a and b which show saturation in  $\beta$  despite significant increases in Neutral Beam Injection (NBI) power. For the shot in red, Figure 1c shows a burst in the Mirnov fluctuation amplitude at  $t=225\text{ms}$ . This  $n = 1$  mode grows with a 0.3-0.5ms growth time and causes a large fractional drop (30%) in the neutron rate as shown in Figure 1d. Since the heating power is fixed during this time, the neutron rate begins to rise again with the previous rate of rise, but then saturates as a long-lived 1/1 mode grows slowly, saturates, and then decays during a duration of 70ms. For the lower  $\beta$  shot in black, the 1/1 mode initial growth time is much longer (2-5ms), and the effect on the neutron rate is much less prompt. In both cases, the presence of the 1/1 mode significantly decreases the rate of rise of the

neutron rate, and apparently results in a lower neutron production rate than would be achieved in the absence of the mode. In both discharges, the 1/1 mode is observed to become unstable when  $q_{min}$  is near 1 (measured without MSE),  $\beta_P > 0.4$ , and  $\beta_N > 4$ .

The central thermal ion temperature is typically 1-3keV in NSTX, so nearly of all the neutron production is from beam-target fusion reactions. The strong correlation between neutron rate and the density of fast ions with energies near the injection energy (80keV) is evident by comparing Figures 2a and b for the highest  $\beta$  discharge of Figure 1. As seen in Figure 2b, the Neutral Particle Analyzer (NPA) [18] count rate for energy near 75keV drops by a factor of two during the first  $n = 1$  mode burst, transiently recovers, and then drops again as the  $n = 1$  instability grows again and then saturates. Figure 2c indicates that a similar drop in fast ion density occurs across most of the energy spectrum as can be seen by comparing the NPA spectrum early in the mode growth phase (black curve) to later times (blue and red curves). Finally, Figure 2c also shows that during the mode saturation phase indicated by the blue and red curves, the low energy ion distribution ( $E < 30keV$ ) reaches a near steady state, whereas increasing fast ion depletion is apparent between energies  $E = 30keV$  and  $E = 80keV$ . From this data, we conclude that the density of fast ions with energy above approximately 30keV drops by a factor of 3 to 5 when the saturated 1/1 mode is present, while the loss rate of lower energy fast ions is smaller. The fast ion confinement in the core is clearly degraded by the mode, and it is therefore likely that any fast-ion stabilization effects are weakened by the onset and saturation of the mode. We therefore conclude that fast-ion stabilization effects are unlikely to be the dominant saturation mechanism for the 1/1 mode unless the fast ions were in fact initially linearly destabilizing.

## 2.2. Sheared toroidal rotation

2.2.1. *Impact on equilibrium force balance* NBI is presently unidirectional on NSTX, and thus far has only been in the co-plasma-current direction to minimize prompt loss of fast ions. Since high- $\beta$  is only routinely achieved with NBI, significant toroidal rotation is nearly always present in NSTX high- $\beta$  discharges. As the toroidal flow speed becomes comparable to the sound speed, centrifugal effects become important [19, 20] and the single-fluid MHD force balance for scalar pressure becomes:

$$\vec{J} \times \vec{B} = \nabla p + \rho \vec{v} \cdot \nabla \vec{v}. \quad (1)$$

Solutions to this total force balance equation depend on various assumptions, such as whether one works in a highly collisional or nearly collisionless limit. Assuming collisional friction forces are sub-dominant to the centrifugal and electrostatic forces [21], the momentum balance equation for each species  $s$  becomes:

$$\vec{J}_s \times \vec{B} = \nabla p_s + \rho_s \vec{v}_s \cdot \nabla \vec{v}_s + Z_s e n_s \nabla \Phi \quad (2)$$

where  $\vec{J}_s$  is the species current density,  $p_s$  is the species scalar pressure,  $\vec{v}_s$  is the species fluid velocity,  $Z_s$  is the species charge number,  $n_s$  is the species density, and  $\Phi$  is the 2D electrostatic potential. Assuming that isotropic species temperatures  $T_s = T_s(\psi)$  and toroidal rotation angular frequencies  $\Omega_{\phi s} = \Omega_{\phi s}(\psi)$  are flux functions (i.e. no poloidal flow), the fact that the component of Equation 2 along  $\vec{B}$  is identically zero yields 2D species density solutions of the form:

$$n_s(\psi, R) = N_s(\psi) \exp(m_s \Omega_{\phi s}^2 (R^2 - R_0^2) / 2k_B T_s - Z_s e \Phi(\psi, \theta) / k_B T_s). \quad (3)$$

Including the angular momentum of the fast ions, treating the fast ions as an isotropic species, and using the quasi-neutrality constraint, the potential variation on a flux surface can be obtained using an iterative solution to the multi-species density equations above. Solutions to these equations generally show good agreement with the measured



electron density profile provided that the modeled fast ion distribution function from TRANSP [22] is not too anisotropic and the discharge is relatively MHD quiescent.

One difficulty with the above formulation of the species densities and pressures is the loss of a simple total equilibrium force balance equation for computing the total plasma current density and poloidal flux. Significant simplification occurs if the electrostatic potential is also treated as a flux function. This yields more approximate solutions to Equation 1 for multiple ion species given by:

$$\vec{J} \times \vec{B} = \sum_s \nabla(n_s T_s(\psi)) + \sum_s m_s n_s \Omega_{\phi s}^2 \nabla(R^2/2) \quad (4)$$

$$n_s(\psi, R) = N_s(\psi) \exp(U(\psi)(R^2/R_0^2 - 1)) \quad (5)$$

$$U(\psi) = P_\Omega(\psi)/P_K(\psi) \quad (6)$$

$$P_\Omega(\psi) = \sum_s N_s(\psi) m_s \Omega_{\phi s}^2 R_0^2 / 2 \quad (7)$$

$$P_K(\psi) = \sum_s N_s(\psi) T_s(\psi) \quad (8)$$

$$0 = \sum_s N_s(\psi) Z_s. \quad (9)$$

Note that for the above solution, the species densities in Equation 5 have the same exponential form in order to satisfy charge neutrality. Equation 5 also shows that in-out asymmetries in the radial profile of the density result from large ratios of centrifugal pressure ( $P_\Omega$ ) to kinetic pressure ( $P_K$ ).

Experimentally, such in-out density asymmetries are often apparent in NSTX Thomson scattering [23] data when the central rotation is sufficiently high. The consistency of the above model equations with the experimental density profiles can be tested by trying to fit the above model to the data. Peaked density profiles provide the most stringent test of the theory, and Figure 3 shows such a comparison for an 800kA  $B_{T0}=4.5$ kG discharge with 6MW of NBI heating. The magnetic reconstruction of this discharge includes the effect of the rotation of the thermal ion species and utilizes electron temperature isosurfaces to help constrain the current profile [24]. Figure 3a

shows that the ion (red) and electron temperatures (blue) are well fit by poloidal flux functions as expected. Figure 3b shows that the carbon impurity ion rotation frequency can be well fit. The green curve in the same figure is the neoclassical deuterium rotation frequency as computed by NCLASS [25] in TRANSP, and typically exceeds the measured carbon rotation. Thus, the local carbon rotation speed may not be representative of the bulk fluid rotation speed if the local ion pressure gradients are sufficiently large [26, 27]. For reference, the ratio of centrifugal to kinetic pressure at the magnetic axis is  $U(\psi = \psi_{axis}) = 0.3$  for this discharge.

Figure 3c plots the fit carbon (red) and computed deuterium (green) density profiles from the model. In this figure, the dashed curves represent the flux-surface-symmetric profiles which are only functions of the poloidal flux, i.e.  $N_C(\psi)$  and  $N_D(\psi)$ , whereas the solid lines represent the 2D profiles  $n_C(\psi, R)$  and  $n_D(\psi, R)$ . Finally, Figure 3d compares the electron density profile (black curve) from the model (i.e.  $n_e(\psi, R)$ ) to the data (diamonds). The model including centrifugal effects is clearly a much better fit to the data than the flux-surface-symmetric profile  $N_e(\psi)$  shown by the dashed curve.

For the model above, the fast ion kinetic pressure and centrifugal pressures are also included. Both pressures are approximated as flux functions for the fast ions, and pressure anisotropy is ignored, as the core anisotropy  $\equiv (p_{\parallel} - p_{\perp})/p$  computed by TRANSP is less than 5% in this relatively high central density discharge. The dotted curve in Figure 3d (between the dashed and solid curves) represents the electron density profile predicted by the model if the fast ion centrifugal pressure is ignored while retaining the fast ion kinetic pressure. For this case, the fast ion centrifugal pressure is relatively small.

In contrast, for a higher temperature, lower density L-mode discharge with  $U(\psi = \psi_{axis}) = 0.2$  and core pressure anisotropy  $\approx 15\%$  shown in Figure 4, the dotted curve

in Figure 4d shows that the fast-ion centrifugal pressure accounts for roughly half the total. Thus, the predicted electron density profile does not agree with the data if the fast ion kinetic pressure is included while ignoring the fast ion centrifugal pressure. Thus, in some cases, it may also be important to include the fast ion contribution to the total toroidal rotation velocity when assessing the impact of rotation on linear stability.

*2.2.2. Impact on stability* The data above clearly shows that centrifugal effects can be important in the equilibrium force balance in NSTX. Centrifugal and flow-shear effects have also been studied previously in the context of internal kink stability [19, 28, 29]. For a high aspect ratio tokamak with circular flux surfaces, the internal kink instability growth rate including sheared rotation can be expressed as [19]:

$$\gamma_0 = -\frac{\pi r_s \omega_A}{\sqrt{3}|q'|R_0^2} \hat{W}_i, \quad \Delta\beta_P^2 \equiv (\beta_p^2 - \frac{13}{144}) \quad (10)$$

$$\hat{W}_i \approx -3r_s|q'|\Delta\beta_P^2 + \left(\frac{2}{\epsilon_V^2} - \frac{1}{\epsilon_\rho^2}\right) \frac{V_0^2}{V_A^2}. \quad (11)$$

Here  $\epsilon_V = L_V/R_0$  and  $\epsilon_\rho = L_\rho/R_0$  where  $L_V$  and  $L_\rho$  are the velocity and density profile scale lengths normalizing the minor radius for parabolic profiles. Thus, high flow speed relative to the Alfvén speed (high  $\frac{V_0}{V_A}$ ) and strong flow shear (small  $\epsilon_V$ ) are potentially strongly stabilizing for the internal kink mode.

The potential stabilizing effect of sheared toroidal flow on the 1/1 mode in NSTX has previously been studied with the M3D code [30]. For typical parameters in NSTX, M3D studies find that nonlinear saturation of the 1/1 mode is not possible via sheared-flow alone for fixed momentum source rate. Rather, as shown in Figure 5, the growth rate is reduced by a factor or 2 to 3, but complete reconnection still occurs in the simulations. As a result of the reconnection, the core pressure and rotation profiles are quickly flattened. Thus, any rotational shear that could stabilize the mode non-linearly

is reduced by the mode itself. However, the simulations also show that if the rotation shear is forced to be maintained during the mode growth, saturation does indeed occur.

Consistent with the simulations with constant momentum input equal to the equilibrium value, rotation flattening is indeed often observed experimentally during the early phase of mode growth. Figure 6 shows the  $\beta$  and mode magnetic field amplitude evolution for two internal-kink unstable discharges. The mode becomes unstable for  $\beta_T$  near 15-20% ( $\beta_N \approx 4$ ) in both discharges. For shot 108104, the NBI heating power increased from 1.6MW to 5MW at  $t=200$ ms. For shot 108103, the NBI heating power increased from 1.6MW to 5MW approximately 30ms later. As a result,  $d\beta/dt$  is 2-3 times higher for 108104 near marginal stability, and this may partly explain the more rapid onset of the mode ( $\tau_g \approx 400-600\mu\text{s}$ ) as compared to 108103 ( $\tau_g \approx 2-5\text{ms}$ ).

Figure 7 shows that the higher  $\beta$  shot from Figure 6 (108103) has 25% higher central rotation speed at mode onset than 108104, and from Equation 11 this could reduce the mode linear growth rate as much as a factor of 1.6 near the marginal  $\beta_P$ . The instability clearly causes rotation angular frequency flattening in both discharges, and the rotation frequency at larger minor radius increases during the flattening consistent with approximate angular momentum conservation during the flattening.

However, Figure 7a suggests that the rotation profile is not completely flattened. Eventually, the core frequency begins increasing as the off-axis rotation frequency drops in the island region and then also reaches a nearly steady-state value of 10kHz near  $R=1.3\text{m}$ . The resultant rotational shear in the non-linear state may aid in the mode saturation. For this shot, the core rotation is maintained at 15kHz or above. In contrast, Figure 7b for shot 108104 shows that the core rotation is lower at mode onset, and is lower following flattening. For this shot, the central rotation never recovers in the presence of the mode, and ultimately the rotation collapses with a flat frequency profile.

As the mode rotation frequency falls below a threshold value near 2kHz, the mode field begins to penetrate the wall and is weakly evident as a rotating mode at the 0.1 Gauss level on the external locked-mode sensors. The mode quickly becomes nearly static ( $f=100-200\text{Hz}$ ) in the lab frame and grows to large amplitude within 1ms near  $t=270\text{ms}$  (1 Gauss on external sensors). The mode then locks with 8 Gauss amplitude within 10ms destroying the remaining thermal and angular momentum confinement. The rapid drop in mode rotation frequency may be the result of the wall drag increasing rapidly with island width and decreasing mode frequency, or may indicate the presence of a forbidden frequency band [31]. For these discharges, comparison of the rotation profiles suggests that if enough rotation and rotational shear is maintained (with a threshold near  $f_{rotation} = 12-15\text{kHz}$ ) following the initial mode growth, the rotation and shear may contribute to the non-linear saturation of the mode.

### *2.3. Island structure and dynamics*

Despite the apparent flattening of the plasma rotation frequency profile following mode onset, the carbon Charge Exchange Recombination Spectroscopy (CHERS) [32] data does not have sufficient time resolution (20ms for the data shown above) to determine when and how quickly the flattening occurs. Faster diagnostics are clearly needed to follow the mode dynamics inside the plasma. The NSTX Ultra-Soft X-Ray (USXR) [33] array measurements have sufficient time resolution (190kHz sampling rate) but are line integrated measurements. However, the emission perturbation from the 1/1 mode is large enough in fluctuation amplitude and spatial extent that important details of the mode structure can be inferred from the USXR data. Indeed, tomographic methods have proven to be a powerful tool in aiding in the determination of the structure of MHD modes [34] in many magnetic fusion devices. Given the spatial resolution of the

present arrays on NSTX, it is beneficial to constrain the SXR emission model of the plasma to more accurately infer the gross characteristics of the mode such as  $q=1$  radius, island width, island poloidal extent, propagation frequency, and estimated magnetic field structure. This model fits the total emission profile in the presence of a large island with a single dominant helicity. The constraints of the island model are described in more detail in Section 4.2 below.

Figure 8a shows line-average emission contours in time versus chord index for shot 108103 near  $t=230$ ms. The chord indices increase from bottom to top of the plasma as viewed from the inboard midplane as shown in Figure 9a. Chords from the upper and lower arrays at the outboard midplane overlap in the plasma core helping to constrain the fit parameters of the island model. Figure 8b shows the best-fit to the chord data using the single helicity island model with the black iso-surface lines overlaid from the measurement to more easily compare the model to measurement. The fitting error is small and is approximately 5-6% for typical cases when the model applies.

Figure 9 shows the inverted emission distribution at constant island phase during the early growth and saturation phases of the island. As seen in Figures 9a-c, the mode grows to nearly full amplitude in approximately 2ms until the full width is roughly equal to the inversion radius. After this comparatively rapid growth phase, Figures 9d-f show the mode width remains essentially unchanged over the next 10ms. At later times, the island width shrinks slowly while the inferred  $q=1$  radius (indicated by the vertical dashed lines) slowly increases.

This evolution is consistent with mode saturation occurring several ms after the initial onset, and the late shrinking of the island width is consistent with the eventual recovery of the core toroidal rotation in Figure 7a. Since complete reconnection does not apparently occur with total expulsion of the hot core from inside the  $q=1$  surface,

it is possible that other effects are needed to explain the rotation flattening shown at  $t=250\text{ms}$  (CHERS integration from 240 to 260ms) in Figure 7a. An alternative mechanism for this flattening is described below.

#### 2.4. Rotation damping from magnetic islands

During the 2004 NSTX run campaign, techniques were adopted from DIII-D [35] to trigger an H-mode transition during the plasma current ramp. The early H-mode transition broadens the plasma pressure and bootstrap current profiles and increases the ramp-up plasma temperature. These effects, combined with higher elongation operation, have allowed significantly longer duration discharges by delaying the onset of deleterious MHD activity associated with the core safety factor being near 1. For instance, the flat-top duration at 1MA has been doubled in NSTX from 0.4s to 0.8 using these techniques. This longer pulse-length allows the fast-ion heating and plasma stored energy to achieve more nearly steady state values at elevated  $q$ . By using such discharges as high  $\beta$  targets either by operating at fixed lower toroidal field (TF) or by ramping down the TF, plasmas with  $\beta \geq 30\%$  are now much more frequently obtained. Nevertheless, the onset and saturation of the 1/1 mode can still limit the  $\beta$  in these discharges by reducing the confinement and rotation either directly or through coupling to other modes.

An example of this is shown in Figure 10 which compares a long-pulse 1.2MA discharge at fixed vacuum toroidal field  $B_{T0} = 0.44\text{T}$  to a high- $\beta$  plasma obtained by ramping  $B_{T0}$  down from 0.44T to 0.29T with otherwise similar discharge conditions. Both discharges have a long-lived  $n=1$  mode present from early in the discharge which appears to be driven unstable by the early H-mode transition. Island model fits to the USXR data for this early mode are most consistent with the presence of an  $m=5$  saturated tearing mode near  $r/a = 0.93$  as shown in the edge emission fluctuation

comparison of Figure 11. However, the edge rotation frequency from CHERS (5kHz) is much lower than the mode frequency (14kHz) from the USXR and magnetic diagnostics, so there is some uncertainty in the eigenfunction being localized at the edge. For instance,  $m = 3$  fits the chord data near  $r/a = 0.7$  reasonably well and more closely agrees with the rotation frequency from CHERS, but cannot reproduce the edge details in the USXR data. Figure 12 plots the inverted emission data for the 5/1 mode indicating an island full-width of 6cm on the outboard side, a very flat emission profile in the plasma core, a region of enhanced emission near the inner island separatrix, and lower emission throughout the island region. The flat emission profile makes detection of internal mode structure difficult. The mode rotation frequency slows from 16kHz to 5kHz from 240ms to 520ms and has a slowly decreasing magnetic fluctuation amplitude throughout this phase to 1 Gauss amplitude by 520ms. The amplitude of the  $n = 1$  mode (possibly with different  $m$  number) begins increasing again near 520-540ms and remains rotating at 5kHz until  $t=560$ ms. For the lower TF shot 112600, near  $t=560$ ms, the  $m/n = 1/1$  mode becomes unstable as evident in the neutron rate drop in Figure 10c and in the appearance of a 15kHz  $n=1$  mode as shown in Figure 13. The frequency spectrogram of Figure 13 also suggests an early coupling between mid-radius and core modes, as the mid-radius mode frequency appears to increase in the early phase of the core mode growth. Later, during the saturation phase of the 1/1 mode, one cannot distinguish between the two modes, as the modes appear to become phase-locked and rotate as a coupled structure.

This coupling is also evident in Figure 14a which indicates the presence of the 1/1 mode (chords 6-14) in addition to a mid-radius mode (chord 3) and edge perturbation (chord 1). The best fit from the single helicity island model (for 1/1) is shown in Figure 14b. For this fit, the radial profile of the helical flux perturbation has been



extended beyond the  $q=1$  radius (at  $R=1.2\text{m}$  at the midplane) to reflect the non-zero displacement outside this radius.

Figure 15 shows that prior to the onset of the  $1/1$  mode, the core rotation profiles for the discharges in Figure 10 are nearly identical despite the significantly lower field of the higher  $\beta$  discharge 112600. Higher spatial and time resolution CHERS data became available during the 2004 experiments, and Figure 15a shows significant rotation damping in the 10ms between  $t=560\text{ms}$  and  $570\text{ms}$  inside the inferred  $q=1$  radius at  $R=1.2\text{m}$ . Interestingly, the rotation is observed to increase outside  $R=1.3$  closer to the plasma edge, while dropping in the intermediate region.

Since the core mode is observed to saturate without complete reconnection, other rotation damping mechanisms are likely at play in the core rotation decay of shot 112600. Electromagnetic torque near the island singular surfaces [36] and enhanced neoclassical toroidal viscosity (NTV) [37, 38] arising from the loss of axisymmetry in the presence of the modes are likely candidates for explaining the rotational braking. Using only the outer channels of the data shown in Figure 14a, the best-fit helicity of the mid-radius perturbation is found to be  $m/n = 2/1$  with an island full-width of  $12\text{cm}$  at the outboard midplane. Figure 16 shows 2D contours of the perturbed radial field of both the  $1/1$  and  $2/1$  islands computed from the island model. Figure 16a shows peak radial fields of  $50\text{-}100$  Gauss in the core with most of the core experiencing a perturbation of at least  $20$  Gauss, while Figure 16b shows that radial field perturbations of  $10\text{-}50$  Gauss are estimated outside the core and approaching the edge. Thus, the magnetic field perturbation from these coupled modes can be expected to extend over most of plasma cross-section with the strongest fields near the core and half-radius. The coupled modes will initially rotate differentially with respect to the sheared plasma rotation, so rotational damping is expected in the plasma core while acceleration could occur at

large minor radius.

Estimates of the rotation profile damping rates have been computed using the perturbed magnetic fields shown in Figure 16. These estimates use a simple cylindrical representation of the mode perturbed field [37] using the flux-surface-average  $B_{\perp}$  of the fields shown in Figure 16. As seen in Figure 17, there is reasonable agreement between the measured rotation damping  $= -\rho R^2 \frac{\partial \Omega_{\phi}}{\partial t}$  and the predicted total damping  $= T_{damping}$  including the effects of axisymmetric fluid viscosity, entrainment of plasma mass in the large 2/1 island, and NTV arising from mode-induced non-axisymmetry. The electromagnetic torques are relatively small compared to the viscous torques for this particular case. The coupled-mode frequency very nearly matches the plasma rotation frequency at the 2/1 surface, so the largest initial differential rotation between mode and plasma occurs in the plasma core. For this reason, the rotation damping contribution from NTV ( $T_{NTV}$  in Figure 17) is only strong in the plasma core ( $R < 1.2\text{m}$ ) where the perturbed fields from the 1/1 mode are large. We infer from this modeling that the net effect of the 1/1 mode NTV torque is to significantly widen the region of flattened rotation relative to what would be induced by the 2/1 mode alone.

While the NTV model is apparently consistent with the observed rotation flattening, the explanation for the decay of the flattened rotation profile is less clear. To better diagnose the low-frequency MHD activity potentially responsible for the rotation decay, an array of 48 new in-vessel magnetic field sensors has been installed in NSTX for the detection of error fields, locked modes, and resistive wall modes. These sensors measure radial field perturbations normal to the primary passive plates and poloidal field perturbations at the ends of the plates both above and below the midplane. There are 12 sensors in each toroidal array allowing toroidal mode number determination ranging from  $n=1$  to 3. The copper plates just behind the radial field sensors strongly filter

any fluctuations above a few tens of Hertz, whereas the poloidal sensors are effectively low-pass filtered above a few kHz but still measure large fluctuations up to 10kHz.

Figure 18a shows the radial field perturbation toroidal mode numbers as determined by these sensor arrays during the rotation decay phase preceding the final  $\beta$  collapse. As is evident from the figure, there is no obvious change in the radial field signals from the time of 1/1 mode onset at 560ms to the final collapse 30ms later. Figure 18b shows similar behavior except the rotating modes appear (aliased by the 5kHz digitizer sampling) starting around 530ms until the collapse phase. In both figures, there is no clear evidence of a slowly growing nearly stationary mode such as a resistive wall mode which might be responsible for the rotation decay.

If no quasi-stationary mode is responsible for the decay, other island effects may be responsible. First, the diffusion and/or loss of fast ions in the presence of a large island structure could reduce the torque applied to the plasma by NBI. Second, Figure 10 indicates that the edge poloidal field perturbation amplitude nearly doubles when the coupled islands are present. Assuming a similar scaling for the island  $B_r$ , this could quadruple the wall torque applied to the mode. Further, as the mode slows, the wall torque would increase since initially  $\omega\tau_{wall} \gg 1$ . Finally, the removal of rotational shear in the plasma core may also contribute to increased angular momentum diffusivity from electrostatic ion turbulence [39, 40].

As for shot 108104 in Figure 7, once the mode rotation frequency falls below 2kHz, it rapidly decreases in frequency, quickly locks to the wall, and then penetrates the passive plates and vacuum vessel. An alternative explanation is that once the rotation falls below this critical value, a resistive wall mode is destabilized [38, 24] and rapidly grows on a 1ms time-scale. Whatever the precise identity of the mode that causes the final disruption, this locked state ultimately induced a vertical displacement event

(VDE) which caused a plasma current disruption in shot 112600. Thus, the operational effects of the 1/1 mode can range from persisting in a relatively benign saturated state to significantly degrading energy and momentum confinement sometimes to the point of island locking and/or RWM destabilization leading to complete collapse of the plasma.

### 2.5. Stabilization from viscous effects

In the linear theory of resistive internal kink mode stability, it has been shown [41] that viscous dissipation is potentially stabilizing for the mode. The resistive treatment is at least partially applicable for NSTX since  $\nu_{ei}\tau_A \approx 0.3$  using an electron-ion collision rate consistent with the neoclassical parallel resistivity. Thus, the collision rate may be competitive with characteristic mode growth rates and may impact even collisionless estimates of the growth-rate [42]. On the other hand, the resistive tearing layer width is much narrower than other characteristic widths thought to control the reconnection, so the simple resistive treatment is unlikely to be relevant to the early non-linear phase [43].

In any case, the stabilization strength of viscous dissipation can be estimated from the linear theory developed for high aspect ratio tokamak plasmas with circular cross section which finds that when the MHD growth rate is less than the ion diamagnetic frequency, the mode complex frequency is given by:

$$\omega \approx \gamma_{MHD}^2/\omega_{di} + (5i/2)\nu_\eta\omega_A^2/|\omega_{di}\hat{\omega}_{*e}| - (i/2)\nu_\mu/\lambda_H^2. \quad (12)$$

In this regime, perpendicular viscosity is stabilizing when  $\hat{D} \geq D_{crit}$  where  $\hat{D} \equiv \nu_\mu/\nu_\eta$ ,  $\nu_\mu$  and  $\nu_\eta$  are viscous and resistive relaxation rates respectively, and  $\hat{D}_{crit} = 5(\omega_A^2/|\omega_{di}\hat{\omega}_{*e}|)\lambda_H^2$ . We note that  $\hat{D} \approx 0.3(m_iT_e/m_eT_i)^{0.5}\beta_e$  implying that perpendicular viscous effects are significantly enhanced by high  $\beta$ . We also note that  $\omega_{*i}/\omega_A = A\beta_i(0)\delta_i/a$  for parabolic profiles where  $A$  is the plasma aspect ratio,  $\beta_i(0)$  is the central ion  $\beta$ ,  $\delta_i$  is the collisionless ion skin depth, and  $a$  is the plasma minor radius. Thus, high

$\beta$  could also enhance the diamagnetic drift stabilization of the internal kink mode.

Applying the equations from Equations 12 to low aspect ratio and shaped plasmas (i.e. beyond their regime of strict applicability), near the time of 1/1 mode onset for discharge 112600 in Figure 10,  $\omega_A \approx 10^6$ ,  $\omega_{*i} \approx 2 \times 10^4$ ,  $\hat{\omega}_{*e} \approx -3 \times 10^4$ , and  $\lambda_H \approx 0.02$ . For these parameters,  $\gamma_{MHD} = 2.3 \times 10^4 \approx \omega_{*i}$ ,  $\hat{D} \approx 2$ , and  $\hat{D}_{crit} \approx 4$ . Consistent with the experiment, for these parameters the mode is estimated to be linearly unstable since  $\gamma_{MHD} > \omega_{*i}/2$  and viscous effects are roughly a factor of 2 too low to provide linear stability. We therefore conclude that unless the perpendicular viscosity is somehow driven anomalously high through nonlinear effects associated with mode growth, it is unlikely that viscous effects play a role in mode saturation. However, the NTV rotation damping process tested above and the kinetic profile data shown in Figure 19 highlight the potentially strong changes in plasma transport and flows induced by magnetic islands that have been both conjectured [44] and observed [45]. Such effects would have to be strong and active over the relevant length scales of the reconnection region of the 1/1 mode which could be as large as  $\rho_{si} \approx 1\text{-}2\text{cm}$  in width and  $\Delta\theta \approx 120^\circ$  in poloidal extent.

### 2.6. Stabilization from island pressure peaking

Nonlinear simulations of the 1/1 mode using the M3D code in the single-fluid resistive MHD approximation [30] did find saturated states under some conditions. Such states were not reproducibly obtained in the simulations however, as these states resulted after several crash cycles and are apparently the result of the pressure becoming locally highest inside the island [46]. Electron cyclotron emission (ECE) measurements of the island electron temperature are not possible in NSTX because of over-dense plasma conditions. However, the mode is sufficiently long-lived in some discharges that several Thomson scattering profiles can be obtained capturing the island structure of the mode. Further,

the CHERS data can provide time-average data to test whether the ion temperature is higher or lower in the island region.

Figure 19 shows the time evolution of these profiles for shot 108103 from Figure 1. Figure 19a at  $t=227\text{ms}$  prior to mode onset shows the electron temperature peaking near the magnetic axis  $R_{axis} = 1.0\text{m}$  as reconstructed by EFIT. During the saturation phase at  $t=243\text{ms}$ , the Thomson scattering system is apparently imaging the mode phase where the hot core has been displaced outwards. At  $t=260\text{ms}$ , the opposite phase is evident with the hot core located on the inboard side with a  $T_e$  flat-spot on the low-field side. By  $t=277\text{ms}$  as the island width is shrinking in the SXR inversions, the central  $T_e$  has largely recovered, and narrow temperature flat-spots are apparent on both sides of the magnetic axis. Figure 19b shows that the electron pressure evolution is very similar to the temperature evolution, as the density profile is relatively flat and changes little with island phase when the mode is present. Figure 19c shows that the ion temperature is initially peaked, flattens and broadens during the early growth phase as does the rotation, and eventually recovers both on-axis and off-axis while remaining depressed near the island region during the mode saturation.

With respect to pressure peaking inside the island, the electron data suggests that the displaced core remains hotter (and with higher pressure) than the island region, and the ion data is consistent with lower ion temperature in the island also. Thus, it appears unlikely that pressure peaking inside the island is responsible for mode saturation.

### 2.7. Ion diamagnetic stabilization

One noteworthy feature of the data in Figure 19b is the obvious displacement of the core at  $t=243\text{ms}$ . The pressure data points outside of  $R=1.3\text{m}$  are nearly identical at  $t=227\text{ms}$  and  $t=243\text{ms}$ , indicating that the displacement outside the core is small -

consistent with the USXR data shown in Figure 8. Further, the local electron pressure gradient is clearly significantly higher in the island inferred X-point region near R=1.25-1.3m at t=243ms. If this pressure gradient enhancement also occurs in the ion channel, quasi-linear enhancement of  $\omega_{*i}$  could also play a role in non-linear saturation of the mode [47]. In the two-fluid theory of the m=1 mode [43], the displacement of the core enhances both the pressure gradient and magnetic shear, and results in a criteria for quasi-linear stability given by:

$$\alpha\omega_{*i}\tau_A > 2q'\sqrt{\lambda_h^2/\bar{q}'^2 + \bar{q}'^2(\rho_s^2 + 5d_e^2)}/2 \quad (13)$$

Here  $\lambda_h$  is the ideal mode layer width,  $\rho_s$  is the ion sound-speed Larmor radius, and  $d_e$  is the collisionless electron skin depth. The pressure gradient enhancement factor  $\alpha = 1 + 2\chi^2$ , the shear enhancement factor  $\bar{q}' = 1 + 6\chi^2$ , and  $\chi = \xi_0/2\pi\lambda_h$  where  $\xi_0$  is the radial displacement of the magnetic axis in the presence of the island. The stability criteria from Equation 13 can be expressed as

$$\alpha\omega_{*i}\tau_A > 2\sqrt{(\gamma_0\tau_A/\bar{q}')^2 + (\bar{q}'q')^2(\rho_s^2 + 5d_e^2)}/2. \quad (14)$$

using the relation

$$\gamma_0\tau_A = q'\lambda_h = \sqrt{3\pi}\epsilon_{q=1}^2\Delta\beta_P^2 \quad (15)$$

which is equivalent to Equations 10 and 11 in the absence of rotation. From these equations, it is evident that at fixed  $\beta$ , the quasi-linear shear enhancement reduces the ideal instability drive, enhances the diamagnetic stabilization, but increases the destabilizing effects of the electron compressibility ( $\rho_s$ ) and inertia ( $d_e$ ). At sufficiently large equilibrium shear  $q'$ , the destabilizing terms dominate and very large  $\omega_{*i}$  is required to stabilize the mode.

Figure 20 plots the normalized displacement of the core predicted by Equation 13 versus the normalized ideal instability growth rate and normalized magnetic shear

$\hat{s} = rdq/dr$  at the  $q=1$  surface. With zero electron diamagnetic drift, Figure 20a shows that for NSTX parameters, there is indeed a range of magnetic shear ( $\hat{s} = 0.1-0.15$ ) where saturated normalized displacements similar to the experimental values of 0.3-0.6 are accessible with ideal linear growth rates well above the nominal threshold of  $\gamma_0/\omega_{*i} = 0.5$ . This implies that mode saturation would occur over a fairly narrow range of magnetic shear and ideal instability drive. However, Equation 13 was derived in the limit of zero electron diamagnetism. When electron diamagnetic effects are included in the quasi-linear dispersion relation, Figure 20b shows that saturation should occur over a wider range of instability drive and shear. For the parameters of the discharge shown, saturation at  $\xi_0/r_{q=1} \approx 0.5$  with  $\gamma_0/\omega_{*i} \gg 0.5$  is possible for  $\hat{s}$  near 0.2 which corresponds to a gradient scale length of approximately 1.4m for  $q$  at the  $q=1$  surface. The predictions of this model will be tested for NSTX in the near-term using magnetic shear measurements from MSE-constrained magnetic reconstructions.

### 3. Summary

Internal kink instabilities have been observed in many of the highest toroidal  $\beta$  discharges of NSTX which have low central safety factor near unity. These modes often cause rotation flattening in the plasma core, can degrade thermal and fast particle confinement, and in some cases contribute to the complete loss of plasma angular momentum and stored energy. In many cases, the modes do not apparently undergo complete reconnection, and in some cases can persist in a saturated state for 10-200 initial growth times. Several candidate saturations mechanisms have been explored and compared qualitatively with experiment.

First, the mode has been observed to significantly increase the fast ion transport and/or loss in the plasma core as evident in the measured neutron rate and NPA



data. Thus, trapped fast ion stabilization is likely reduced, although it is possible that the stabilization is actually enhanced at larger minor radius if the ions are moved from the core but not lost. Rotational shear has been shown theoretically to reduce the growth rate of the internal kink mode, and this may contribute to the relatively slow growth rate of the mode near marginal stability when the central toroidal flow speed approaches the Alfvén speed. Non-linearly, the mode appears to flatten the rotation profile in simulations with M3D and in the experiment, so rotational shear is an unlikely mode saturation mechanism. This rotation flattening is observed even with only partial reconnection, i.e. no ejection of the hot plasma core. However, inside the  $q=1$  surface, the mode non-axisymmetric magnetic field appears to be large enough to cause rotation flattening from enhanced neoclassical toroidal viscosity. In situations where the core mode couples non-linearly to another island at larger minor radius, the rotation flattening can extend to even larger minor radius. In this state, the rotational collapse across most of the plasma can occur leading to plasma disruption either through island locking or destabilization of the resistive wall mode.

Perpendicular viscous effects have also been shown theoretically to reduce internal kink growth rates, and these effects should be enhanced at high  $\beta$ . These effects do not appear sufficiently strong to explain the non-linear saturation behavior unless the island itself leads to an enhanced anomalous viscosity in the reconnection region. Pressure peaking inside the island could also lead to mode stabilization, but appears inconsistent with the available kinetic pressure profile data inside the 1/1 island. Finally, diamagnetic effects are enhanced at high  $\beta$ , and for a range of magnetic shear values, saturated island states with instability drive significantly above the linear diamagnetic stabilization threshold may be possible. Nonlinear diamagnetic stabilization can be evaluated more quantitatively once magnetic shear measurements become available in

the near term. Overall, in the highest toroidal  $\beta$  discharges of NSTX, the onset of the 1/1 mode appears to reduce many of the linearly stabilizing influences on mode growth thereby making the non-linear saturation of the mode difficult to explain.

## 4. Appendix

### 4.1. Flux and field in the single helicity magnetic island model

The magnetic field of the island equilibrium can be computed perturbatively by expanding about an axisymmetric equilibrium. The total magnetic field in the plasma can be expressed as  $\vec{B} = \nabla \times \vec{A}$  where gauge freedom allows the vector potential  $\vec{A}$  to be expressed as  $\vec{A} = \psi_p \nabla \phi - \psi_t \nabla \theta$ . Here  $\phi$  is the (toroidal) angle in a right-handed  $R, \phi, Z$  cylindrical coordinate system,  $\theta$  is a poloidal angle coordinate in the  $R, Z$  plane,  $\psi_p$  is the total (equilibrium plus perturbed) poloidal flux function, and  $\psi_t$  is the total toroidal flux function. In the absence of perturbations, these flux functions are functions of the equilibrium poloidal flux  $\psi \equiv RA_\phi(R, Z)$  only. Specifically,  $\psi_p = \psi$  and  $\psi_t = \int q(\psi) d\psi$ . Dealing with an island of a single helicity, it is convenient to introduce the helical coordinate  $\alpha = \phi - q_s \theta$  where  $q_s$  is the safety factor of the singular surface at which the mode is resonant. This coordinate satisfies  $\nabla \alpha \cdot \vec{B} = 0$  where  $q(\psi) = q_s$ . Perturbed magnetic fields proportional to gradients of this coordinate therefore minimize field-line bending at the mode-rational surface and favor mode instability.

With the introduction of this helical coordinate, the total magnetic field can be expressed as  $\vec{B} = \nabla \psi_p \times \nabla \alpha - \nabla \psi_h \times \nabla \theta$  where the helical flux is defined as:

$$\psi_h \equiv \psi_t - q_s \psi_p \tag{16}$$

To compute the total field in the presence of the island, we now *assume* the total poloidal and toroidal fluxes can be expressed as functions of  $\psi$  and  $\alpha$  alone, i.e.  $\psi_t = \psi_t(\psi, \alpha)$

and  $\psi_p = \psi_p(\psi, \alpha)$ . The total magnetic field then becomes:

$$\vec{B} = \nabla\psi \times \nabla\phi \partial_\psi\psi_p - \nabla\phi \times \nabla\theta \partial_\alpha\psi_h - \nabla\psi \times \nabla\theta \partial_\psi\psi_t \quad (17)$$

From this equation, it is clear that the  $\nabla\psi \cdot \vec{B}$  (radial) component of the magnetic field comes only from the helical flux, and that this component is zero in the axisymmetric system as required. Further, the equilibrium helical flux  $\psi_{h0}(\psi) \equiv \int_{\psi_s}^{\psi} (q(\psi') - q_s) d\psi'$  is zero at the resonant surface, making this flux useful for perturbative expansions about the equilibrium. Perhaps most importantly,  $\nabla\psi_h \cdot \vec{B} = \nabla\alpha \cdot \nabla\psi_h \times \nabla\psi_p = 0$  by construction even in the perturbed system. This implies that  $\psi_h$  can uniquely label magnetic surfaces even in the presence of a magnetic island provided the flux perturbations take the form assumed above.

The detailed structure of the flux and field inside the island depends sensitively on the plasma physics assumed, but outside the island, the field structure should be well approximated by ideal MHD. This implies that outside the island, the perturbed vector potential  $\delta\vec{A} \approx \vec{\xi} \times \vec{B}_0$  where  $\vec{\xi}$  is the plasma displacement and  $\vec{B}_0$  is the equilibrium magnetic field. From this relation, it follows that  $\delta\psi_p = -\vec{\xi} \cdot \nabla\psi$  and that  $\delta\vec{A} = (\nabla\phi - q\nabla\theta)\delta\psi_p$ . This allows the perturbed poloidal flux outside the island to be related to the perturbed helical flux via  $\delta\psi_p = \delta\psi_h/(q - q_s)$ . This relation demonstrates both the singular behavior and odd parity of the normal displacement near the resonant (singular) surface for an even and finite helical flux perturbation at this surface.

Since an infinite normal displacement is nonphysical, the perturbed poloidal flux is assumed to vary across the singular layer as:

$$\delta\psi_p(\psi, \alpha) = f(\psi)\delta\psi_h(\psi, \alpha)/(q(\psi) - q_s) \quad (18)$$

where  $f(\psi) = 1 - \exp(-\alpha^2 x^2)$ ,  $x = \rho - \rho_s$ ,  $\rho = \hat{\psi}^{1/2}$ ,  $\hat{\psi}$  is the normalized equilibrium poloidal flux, and  $\alpha = 2/w_p$  where  $w_p$  is the normalized minor radial width of the poloidal flux variation across the singular surface located at  $\rho = \rho_s$ . The perturbed

helical flux of the single-helicity island is further assumed to be separable in the radial and helical coordinates, specifically:

$$\delta\psi_h = A(\psi)\cos(n\alpha) \quad (19)$$

where the integer  $n$  is the toroidal mode number of the tearing mode. With this formulation, tearing modes with  $m/n = q_s$  where  $m$  is the integer poloidal mode number will then generate resonant perturbations to the radial magnetic field and create magnetic islands.

The model amplitude profile form used is  $A(\psi) \propto \rho^m(1 - \rho)^{\frac{m(1-\rho_s)}{\rho_s}}$  (for  $m \geq 2$ ) which scales as  $\rho^m$  for small  $\rho$  consistent with cylindrical theory, has maximum value at  $\rho = \rho_s$ , and is zero at the plasma boundary. For  $m=1$ , the model amplitude profile form used is  $A(\psi) \propto \hat{\rho}_s(1 - \hat{\rho}_s)$  where  $\hat{\rho}_s = \rho/\rho_s$  for  $\rho \leq \rho_s$  and  $A(\psi) = 0$  for  $\rho > \rho_s$ . The amplitude of the  $\delta\psi_h$  profile is then adjusted to generate a magnetic island at the chosen rational surface  $\rho_s$  of full width  $\Delta\rho = w$ . With the perturbed helical flux function and poloidal flux function variation width  $w_p$  specified, equations 16–19 can be used to calculate the field from a single tearing mode anywhere in the equilibrium plasma. The profile for the perturbed helical flux could also be obtained from a code such as PEST-3 [48] and could include such effects as non-zero edge displacement and calculations of the mode field in the vacuum region.

#### 4.2. Magnetic island emissivity model constraints

For the tomographic inversions discussed above, the SXR emission is assumed to be a function of the total helical flux alone. Emissivity basis functions of the normalized total helical flux both inside and outside the island are applied, and line integrals through each basis function are computed numerically. The line-average measurements of the SXR emission are then used to determine the 3D emissivity profile using SVD techniques. The

island width and poloidal extent are scanned to find the best fit to the data. It is also necessary to scan the  $q=1$  radius for the 1/1 mode as internal  $q$ -profile measurements are presently unavailable. The helical flux profile is a direct byproduct of this inversion process and can be used to estimate the magnetic field perturbation from the island as described above in Section 4.1.

## Acknowledgments

This work was supported by the United States Department of Energy under contract numbers DE-AC02-76CH03073 (PPPL) and grant numbers DE-FG02-99ER54524 (CU), DE-FG02-99ER54523 (JHU).

## References

- [1] PENG, Y.-K. M. and STRICKLER, D. J., Nucl. Fus. **26** (1986) 769.
- [2] ONO, M., KAYE, S., PENG, Y.-K., BARNES, G., BLANCHARD, W., et al., Nucl. Fus. **40** (2000) 557.
- [3] SYKES, A., AKERS, R. J., APPEL, L. C., ARENDS, E. R., CAROLAN, P. G., et al., Nucl. Fus. **41** (2001) 1423.
- [4] MAINGI, R., BELL, M. G., BELL, R. E., BUSH, C. E., FREDRICKSON, E. D., et al., Phys. Rev. Lett. **88** (2002) 035003.
- [5] AKERS, R. J., COUNSELL, G. F., SYKES, A., APPEL, L. C., ARENDS, E. R., et al., Phys. Rev. Lett. **88** (2002) 035002.
- [6] MENARD, J. E., BELL, M. G., BELL, R. E., FREDRICKSON, E. D., GATES, D. A., et al., Nucl. Fus. **43** (2003) 330.
- [7] GATES, D. and the NSTX National Research Team, Phys. Plasmas **10** (2003) 1659.
- [8] LAO, L. L., St. John, H., STAMBAUGH, R. D., KELLMAN, A. G., and PFEIFFER, W., Nucl. Fus. **25** (1985) 1611.
- [9] SABBAGH, S. A., KAYE, S. M., MENARD, J., BELL, M., BELL, R., et al., Nucl. Fus. **41** (2001) 1601.

- [10] SABBAGH, S. A., BELL, R. E., BELL, M. G., BIALEK, J., GLASSER, A. H., et al., *Phys. Plasmas* **9** (2002) 2085.
- [11] LEVINTON, F., Private communication.
- [12] FREDRICKSON, E. D., GORELENKOV, N., CHENG, C. Z., BELL, R., DARROW, D., et al., *Phys. Rev. Lett.* **87** (2001) 145001.
- [13] FREDRICKSON, E. D., GORELENKOV, N. N., and MENARD, J., *Phys. Plasmas* **11** (2004) 3653.
- [14] FREDRICKSON, E. D., CHENG, C. Z., DARROW, D., FU, G., GORELENKOV, N. N., et al., *Phys. Plasmas* **10** (2003) 2852.
- [15] COPPI, B., MIGLIUOLO, S., PEGORARO, F., and PORCELLI, F., *Phys. Fluids B* **2** (1990) 927.
- [16] CAMPBELL, D. J., START, D. F. H., WESSON, J. A., BARTLETT, D. V., BHATNAGAR, V. P., et al., *Phys. Rev. Lett.* **60** (1988) 2148.
- [17] BERNABEI, S., BELL, M. G., BUDNY, R. V., FREDRICKSON, E. D., GORELENKOV, N. N., et al., *Phys. Rev. Lett.* **84** (2000) 1212.
- [18] MEDLEY, S. and ROQUEMORE, A., *Rev. Sci. Instrum.* **75** (2004) 3625.
- [19] WAELBROECK, F. L., *Phys. Plasmas* **3** (1996) 1047.
- [20] GUAZZOTTO, L., BETTI, R., MANICKAM, J., and KAYE, S., *Phys. Plasmas* **11** (2004) 604.
- [21] ROMANELLI, M. and OTTAVIANI, M., *Plasma Phys. and Contr. Fus.* **40** (1998) 1767.
- [22] GOLDSTON, R. J., MCCUNE, D. C., and TOWNER, H. H., *J. Comput. Phys.* **43** (1981) 61.
- [23] JOHNSON, D., BRETZ, N., LEBLANC, B., PALLADINO, R., LONG, D., et al., *Rev. Sci. Instrum.* **70** (1999) 776.
- [24] SABBAGH, S. A., *Nucl. Fus.* (2004), In preparation.
- [25] HOULBERG, W. A., SHAIN, K. C., HIRSHMAN, S. P., and ZARNSTORFF, M. C., *Phys. Plasmas* **4** (1997) 3230.
- [26] ERNST, D. R., BELL, M. G., BELL, R. E., BUSH, C. E., CHANG, Z., et al., *Phys. Plasmas* **5** (1998) 665.
- [27] BAYLOR, L. R., BURRELL, K. H., GROEBNER, R. J., HOULBERG, W. A., ERNST, D. P., et al., *Phys. Plasmas* **11** (2004) 3100.
- [28] WAHLBERG, C. and BONDESON, A., *Phys. Plasmas* **7** (2000) 923.
- [29] GRAVES, J. P., SAUTER, O., and GORELENKOV, N. N., *Phys. Plasmas* **10** (2003) 1034.

- [30] PARK, W., BRESLAU, J., FU, J. C. G. Y., JARDIN, S. C., KLASKY, S., et al., Nucl. Fus. **43** (2003) 483.
- [31] GATES, D. A. and HENDER, T. C., Nucl. Fus. **36** (1996) 273.
- [32] BELL, R., LEBLANC, B., BOURDELLE, C., ERNST, D., FREDRICKSON, E., et al., Kinetic profiles in NSTX plasmas, Technical Report 3591, PPPL, 2001.
- [33] STUTMAN, D., FINKENTHAL, M., SOUKHANOVSKII, V., MAY, M., MOOS, H., et al., Rev. Sci. Instrum. **70** (1999) 572.
- [34] JANICKI, C., DECOSTE, R., and SIMM, C., Phys. Rev. Lett. **62** (1989) 3038.
- [35] GREENFIELD, C. M., MURAKAMI, M., FERRON, J. R., WADE, M. R., LUCE, T. C., et al., Phys. Plasmas **11** (2004) 2616.
- [36] FITZPATRICK, R., Nucl. Fus. **33** (1993) 1049.
- [37] LAZZARO, E., BUTTERY, R. J., HENDER, T. C., ZANCA, P., FITZPATRICK, R., et al., Phys. Plasmas **9** (2002) 3906.
- [38] SABBAGH, S. A., BIALEK, J. M., BELL, R. E., GLASSER, A. H., LEBLANC, B. P., et al., Nucl. Fus. **44** (2004) 560.
- [39] KOTSCHENREUTHER, M., DORLAND, W., LIU, Q., ZARNSTORFF, M., MILLER, R., et al., Nucl. Fus. **40** (2000) 677.
- [40] STUTMAN, D., FINKENTHAL, M., BELL, R. E., KAYE, S. M., LEBLANC, B. P., et al., Phys. Plasmas **10** (2003) 4387.
- [41] PORCELLI, F. and MIGLIUOLO, S., Phys. Fluids **29** (1986) 1741.
- [42] PORCELLI, F., Phys. Rev. Lett. **66** (1991) 425.
- [43] ZAKHAROV, L. and ROGERS, B., Phys. Fluids B **4** (1992) 3285.
- [44] SHAIN, K. C., Phys. Rev. Lett. **87** (2001) 245003.
- [45] IDA, K., OHYABU, N., MORISAKI, T., NAGAYAMA, Y., INAGAKI, S., et al., Phys. Rev. Lett. **88** (2002) 015002.
- [46] PARK, W., MONTICELLO, D. A., and CHU, T. K., Phys. Fluids **30** (1987) 285.
- [47] ROGERS, B. and ZAKHAROV, L., Phys. Plasmas **2** (1995) 3420.
- [48] PLETZER, A., BONDESON, A., and DEWAR, R. L., J. Comput. Phys. **115** (1994) 530.

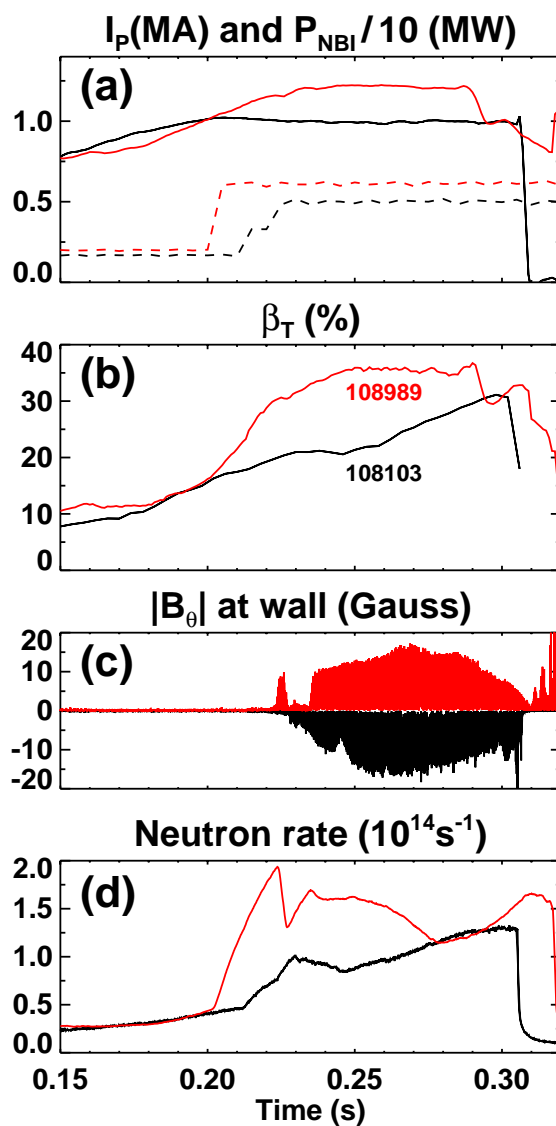


**Figure 1.** (a) Plasma current and NBI heating power, (b) toroidal beta, (c) integrated edge Mirnov amplitudes at vessel wall, and (d) neutron rates for two high beta NSTX discharges whose confinement and beta are limited by saturated 1/1 islands in the plasma core.



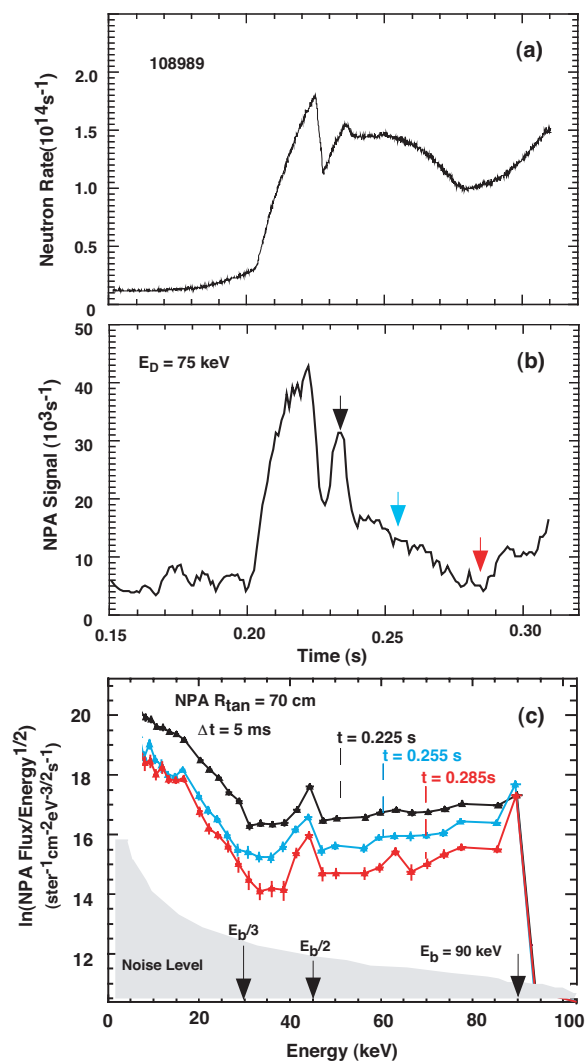


**Figure 2.** (a) Neutron rate versus time, (b) NPA count rate at deuteron energy = 75 keV versus time, and (c) energy distribution function for the three times highlighted in (b) for shot 108989 from Figure 1.

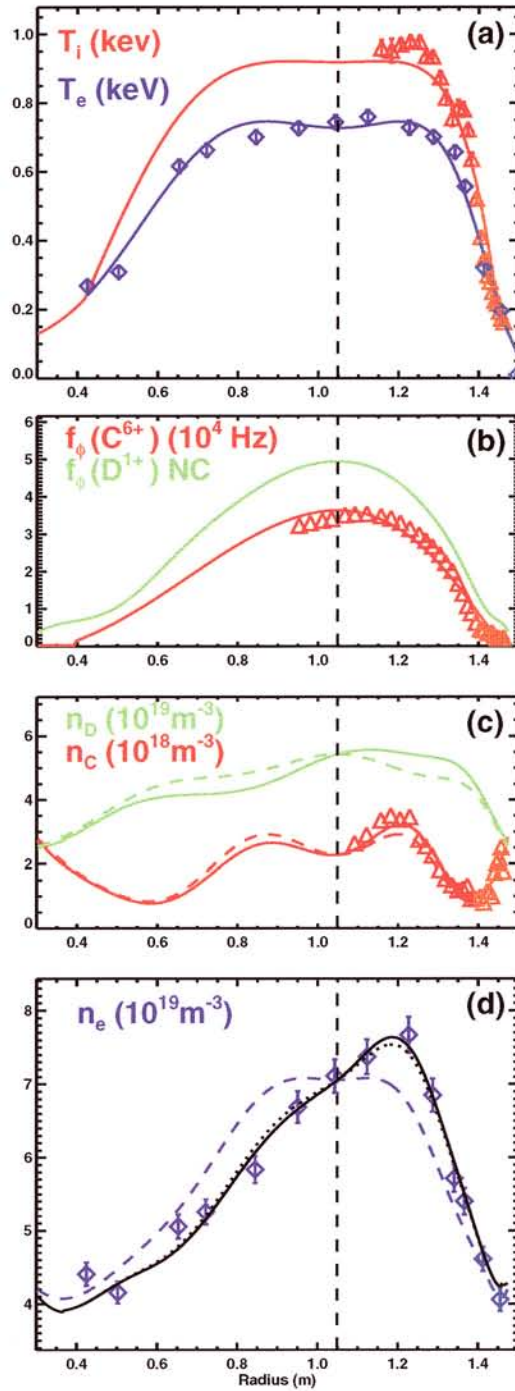


**Figure 3.** Kinetic profiles for discharge 112546 at  $t=547\text{ms}$ . (a) Poloidal flux function fits to ion (red) and electron (blue) temperature profiles, (b) poloidal flux function fits to carbon and deuterium (neoclassical) toroidal rotation frequencies, (c) carbon (red) and deuterium (green) number density profiles, and (d) electron density profiles. Dashed curves in the figures correspond to the profiles which are functions of poloidal flux only, and vertical dashed lines represent the magnetic axis.

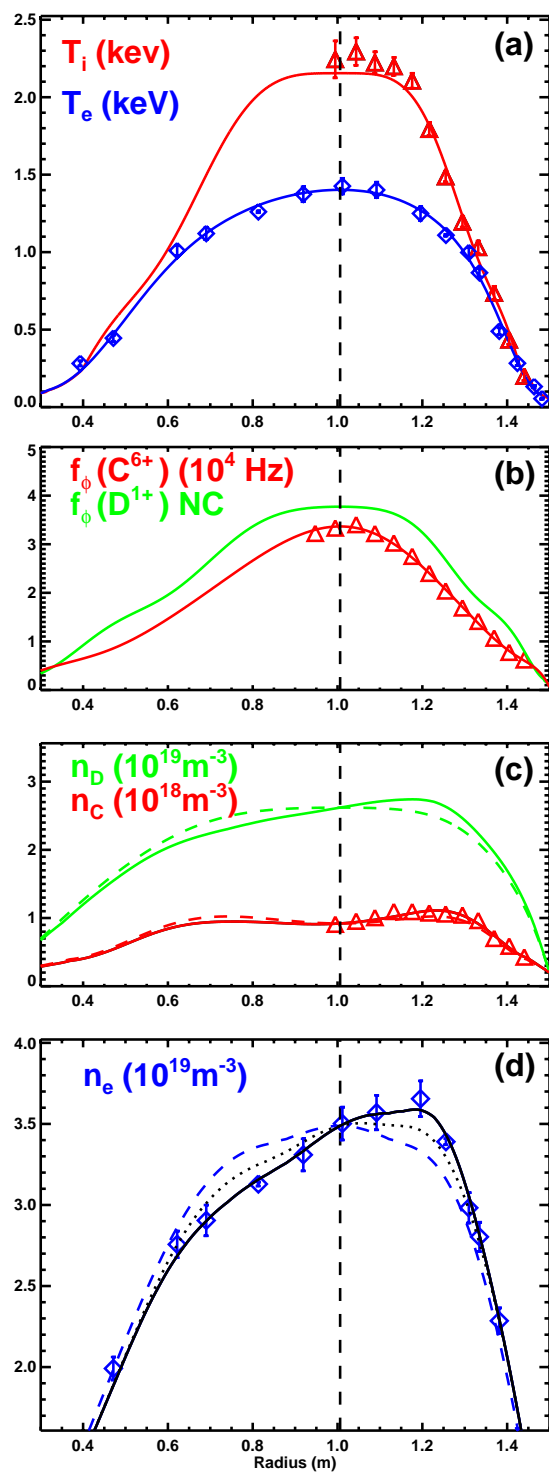


**Figure 4.** Kinetic profiles for discharge 107540 at  $t=330$ ms. Figure labels are the same as those in Figure 3.

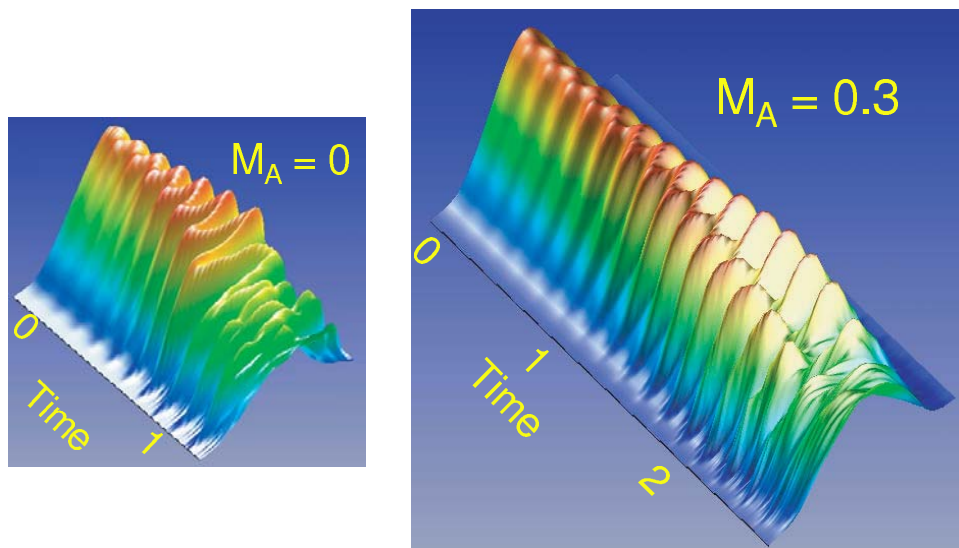


**Figure 5.** Simulated SXR signals from M3D for an equilibrium with 24% toroidal beta with  $q_{min} = 0.85$  and  $\rho(q = 1) = 0.45$  for on-axis Alfvén Mach numbers  $M_A = 0.0$  and 0.3. The growth rate of the higher  $M_A$  case is reduced by a factor of 2-3 relative to zero plasma rotation.

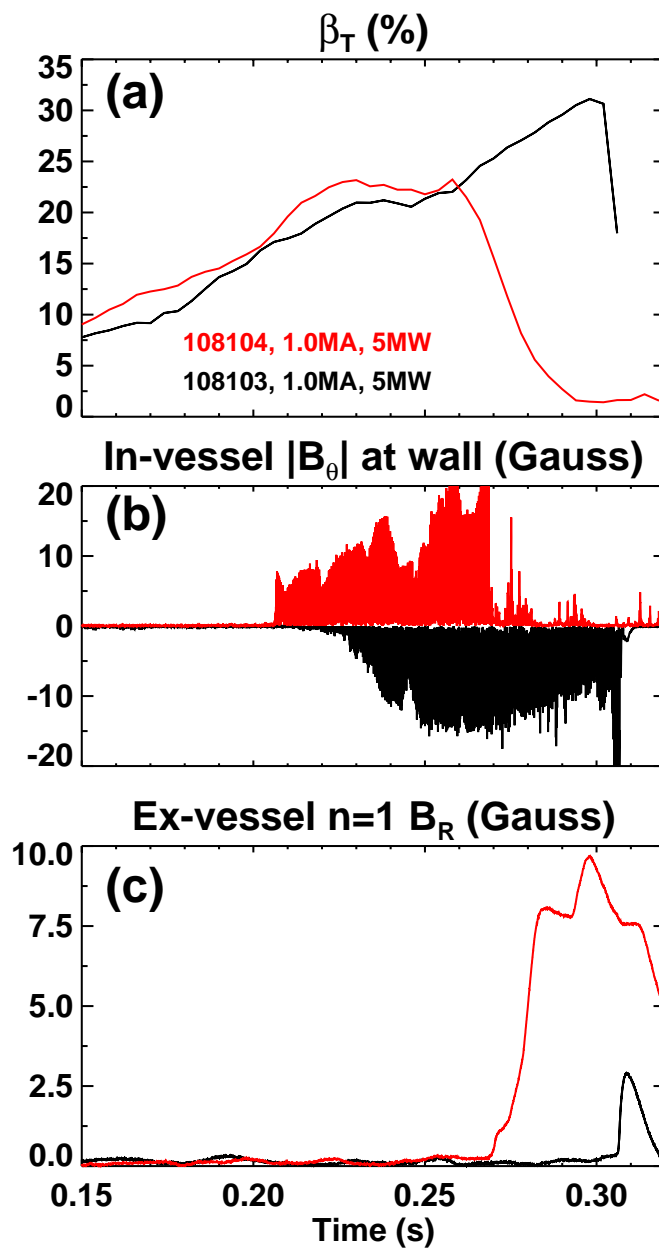


**Figure 6.** (a) Toroidal beta, (b) integrated edge Mirnov amplitudes at vessel wall, and (c) ex-vessel  $n=1$  radial field amplitude for discharges whose thermal confinement and core rotation are reduced by saturated  $1/1$  modes.

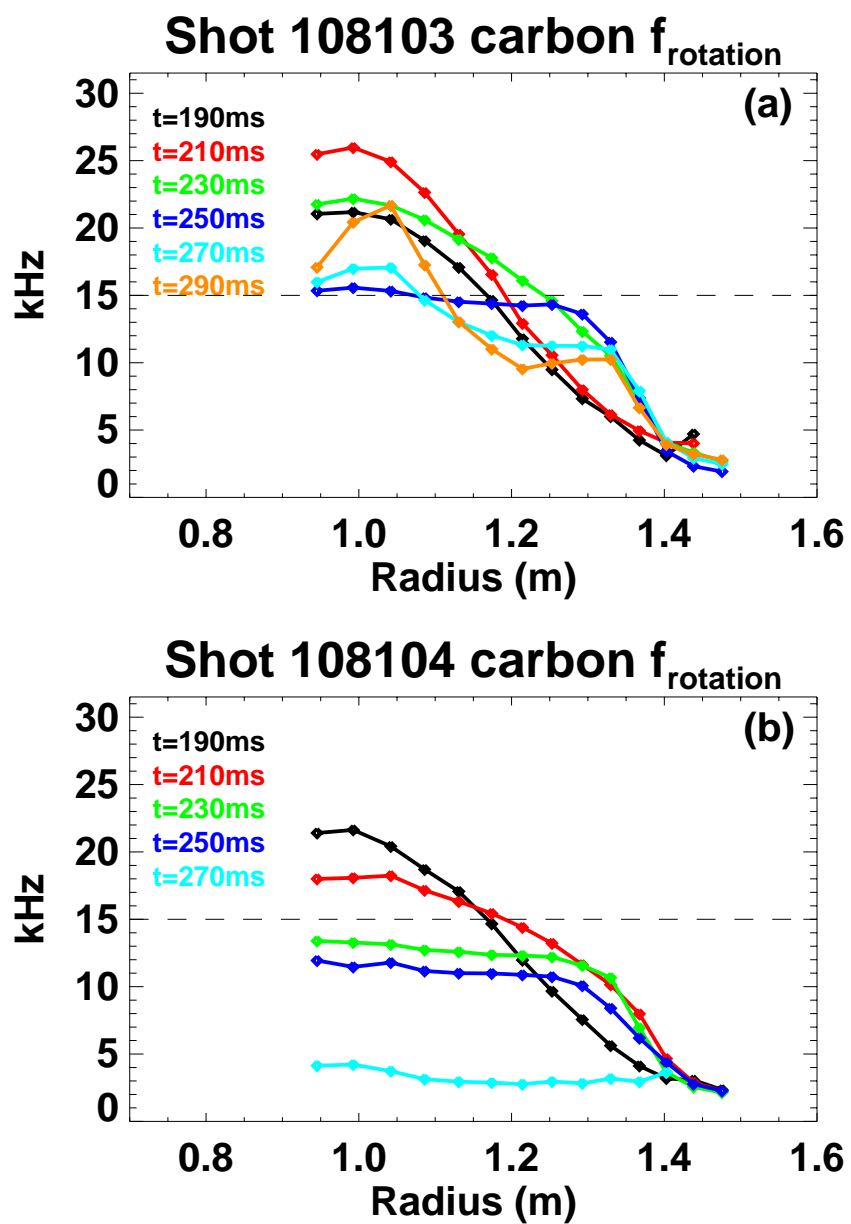


**Figure 7.** Rotation profile evolution for discharges (a) 108103 and (b) 108104 from Figure 6.

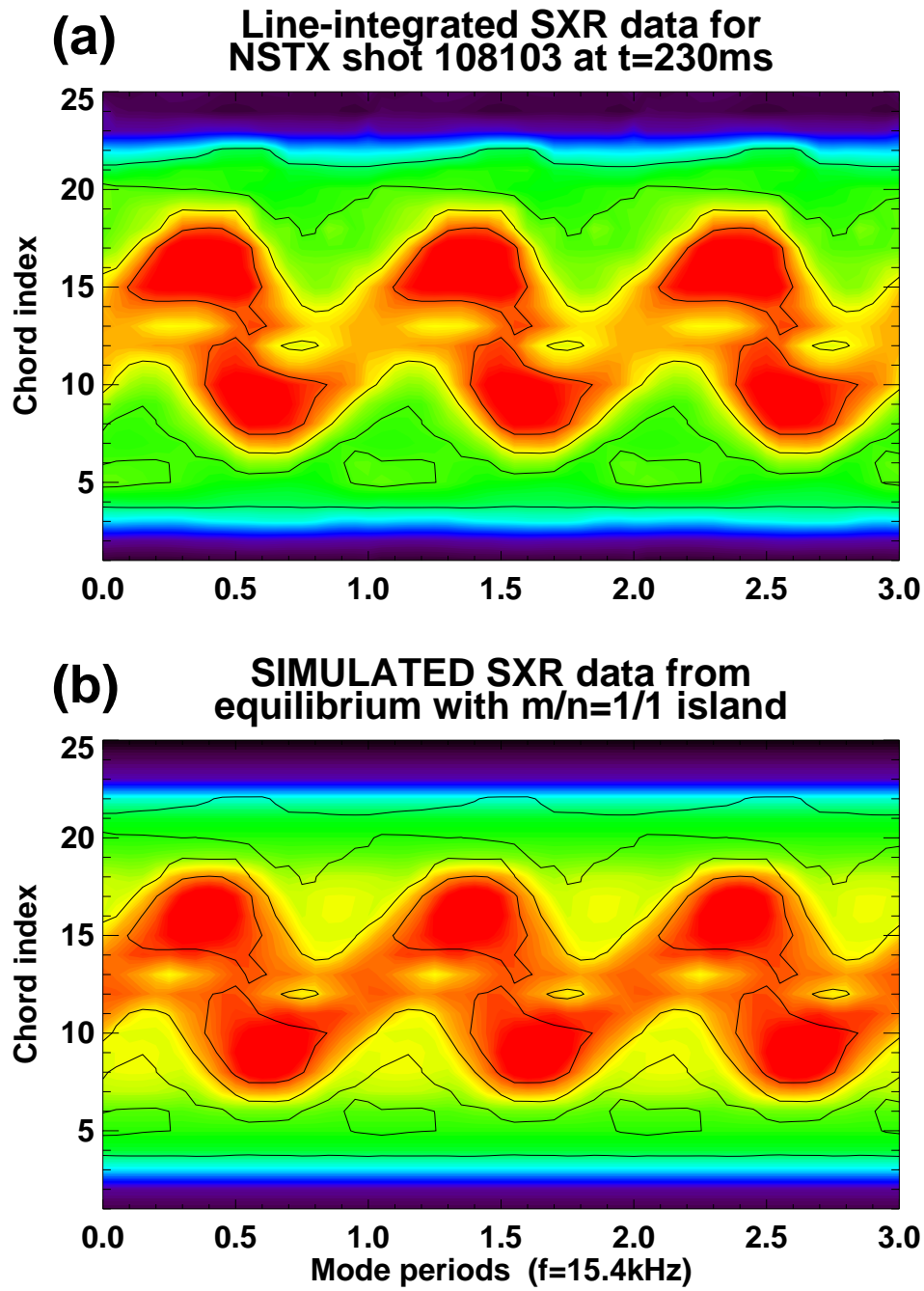


**Figure 8.** (a) Contours of USXR line-average emission in time versus chord index with a large  $1/1$  mode present for shot 108103, and (b) best-fit to the emission data using the single-helicity island model. The black contour lines are from the measurements in both figures.

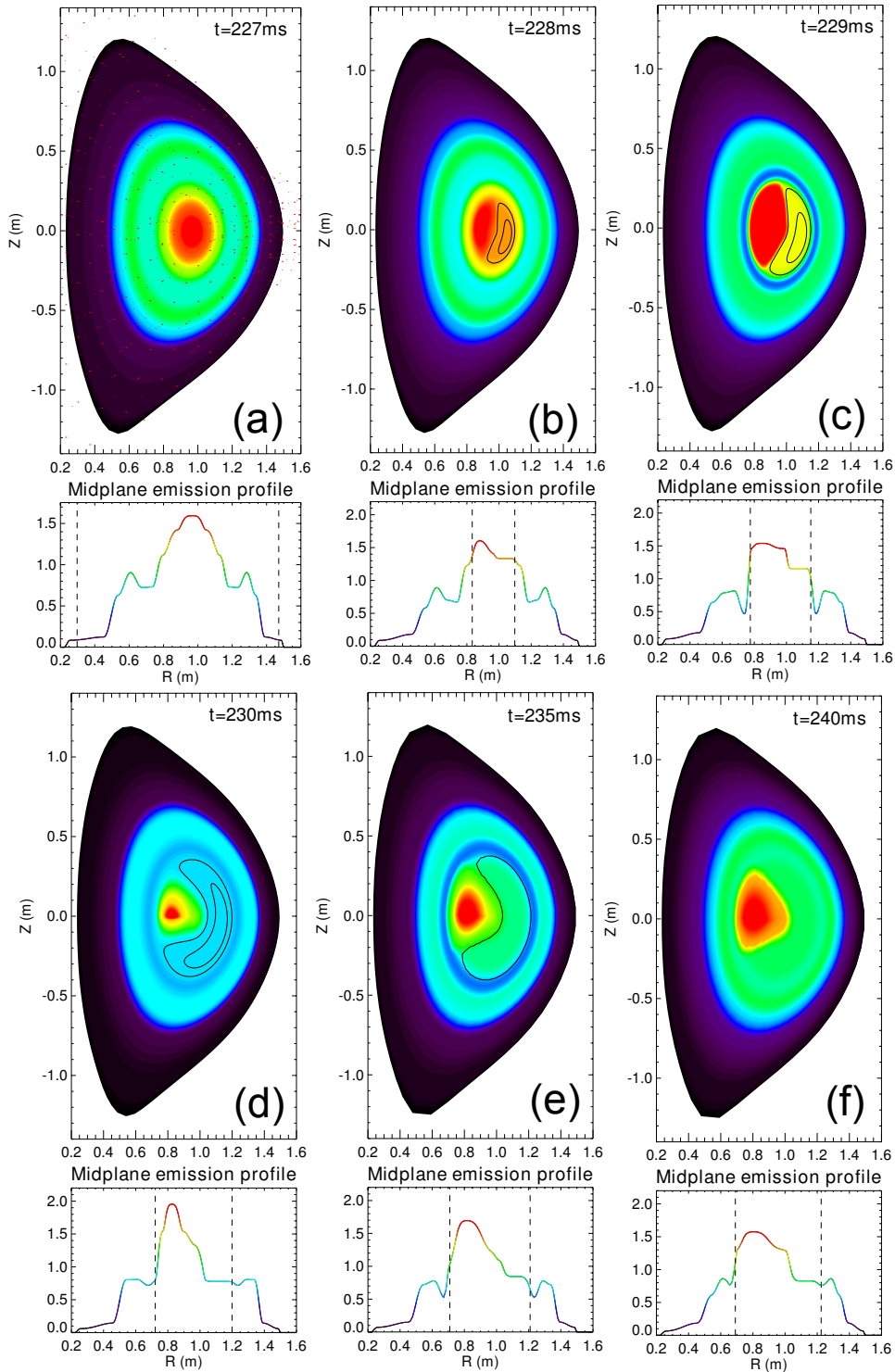


**Figure 9.** Evolution of reconstructed island emission during early growth (a-c) and saturation phase (d-f) for shot 108103. Dashed vertical lines in the midplane emission plots indicate the position of the  $q=1$  surface inferred from the model.



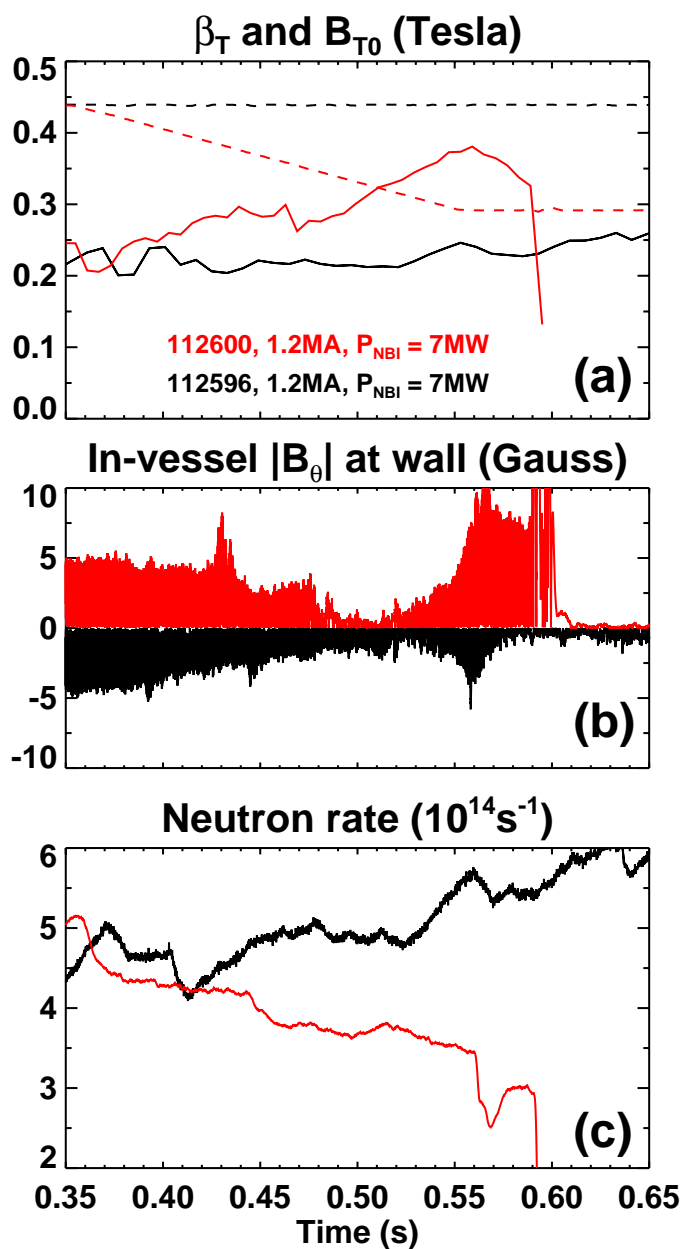


**Figure 10.** (a) Toroidal  $\beta$  and vacuum toroidal field (dashed), (b) magnetic fluctuation amplitude, and (c) neutron rate for 1.2MA discharges 112596 and 112600.

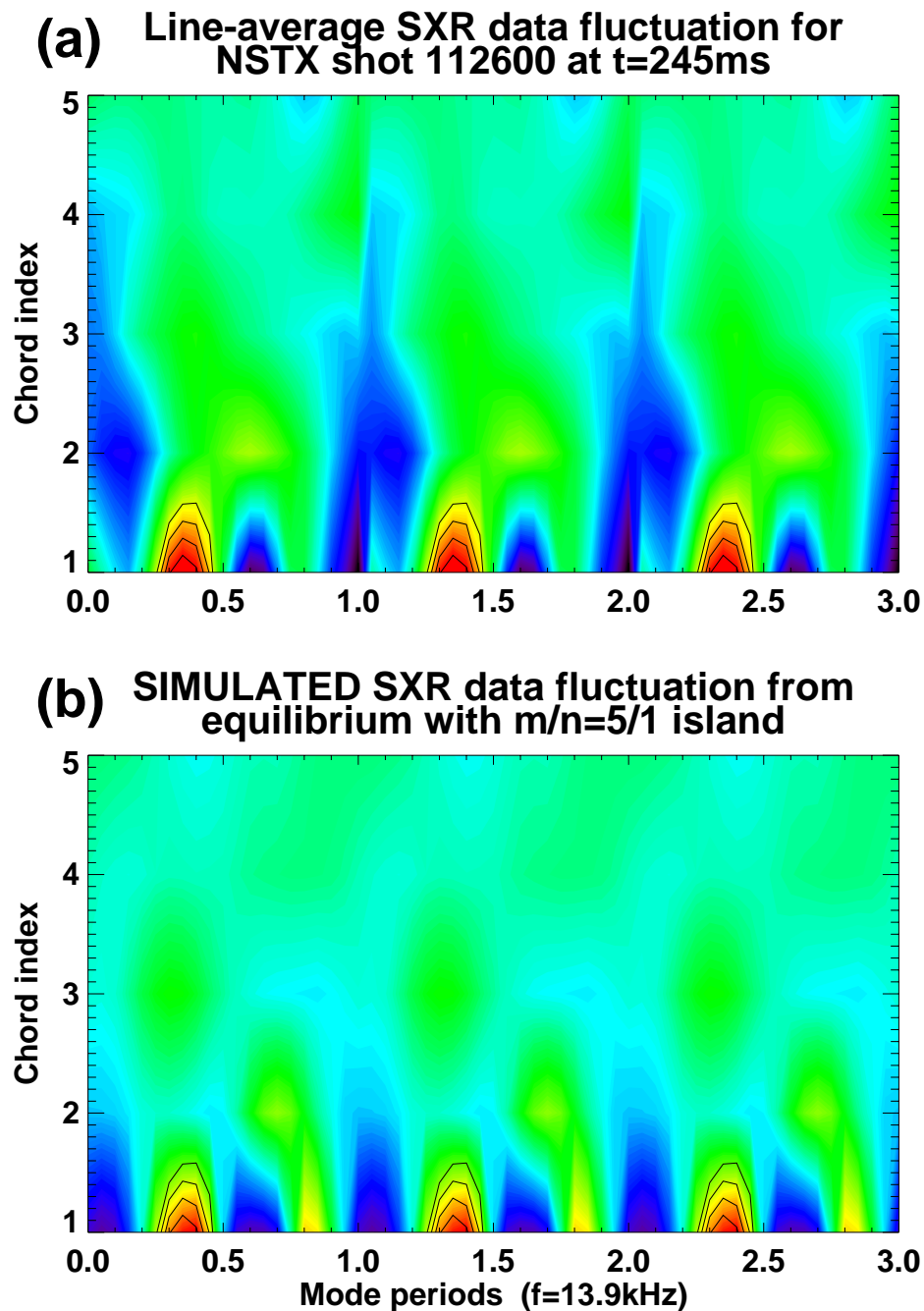


**Figure 11.** (a) Contours of USXR line-average emission fluctuation in time versus edge chord index for shot 112600 at  $t=245\text{ms}$ , and (b) best-fit to the emission data using the single-helicity island model with  $m/n = 5/1$  and island radius at the  $q=5$  surface from the equilibrium reconstruction. The black contour lines are from the measurements in both figures.

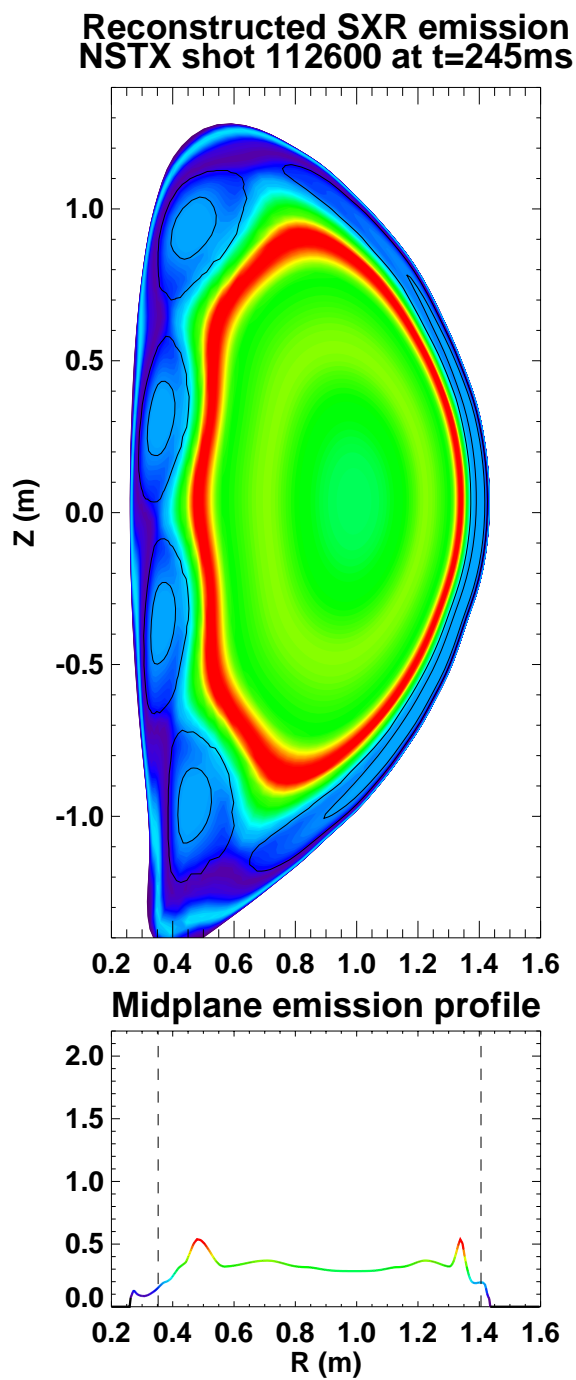


**Figure 12.** Inverted USXR emission contours showing the structure of the saturated 5/1 island inferred from the fit shown in Figure 11.

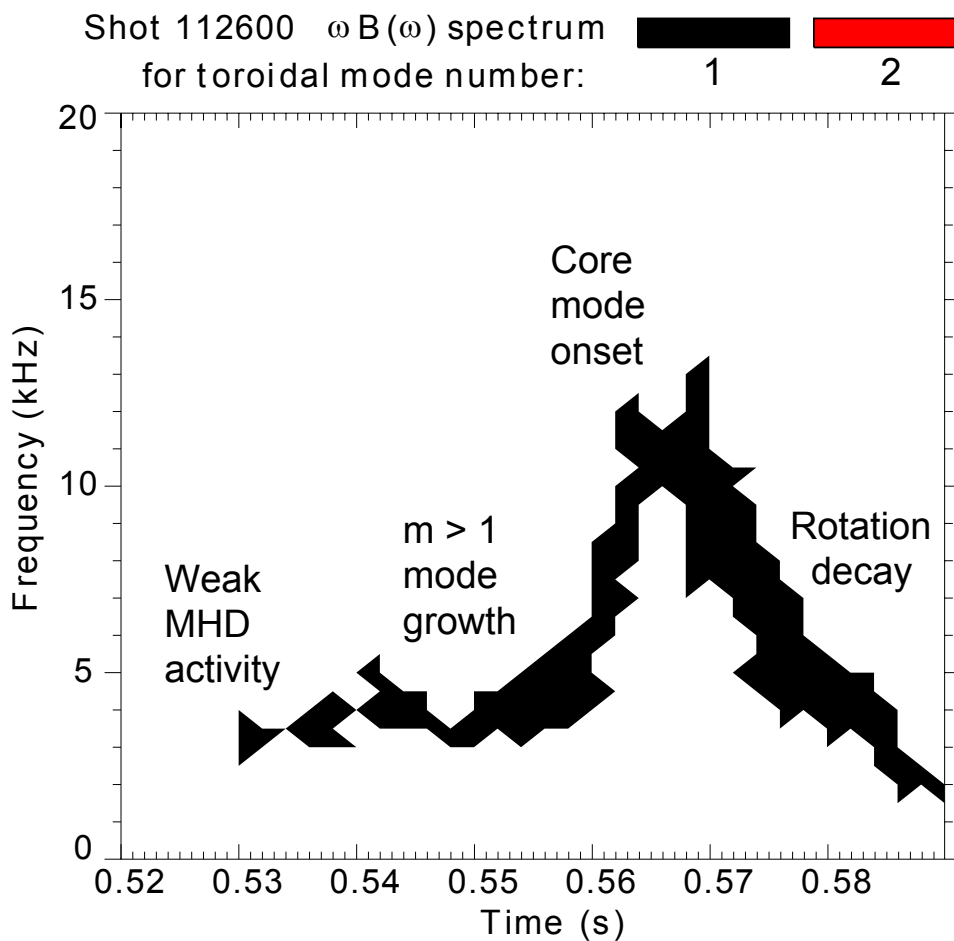
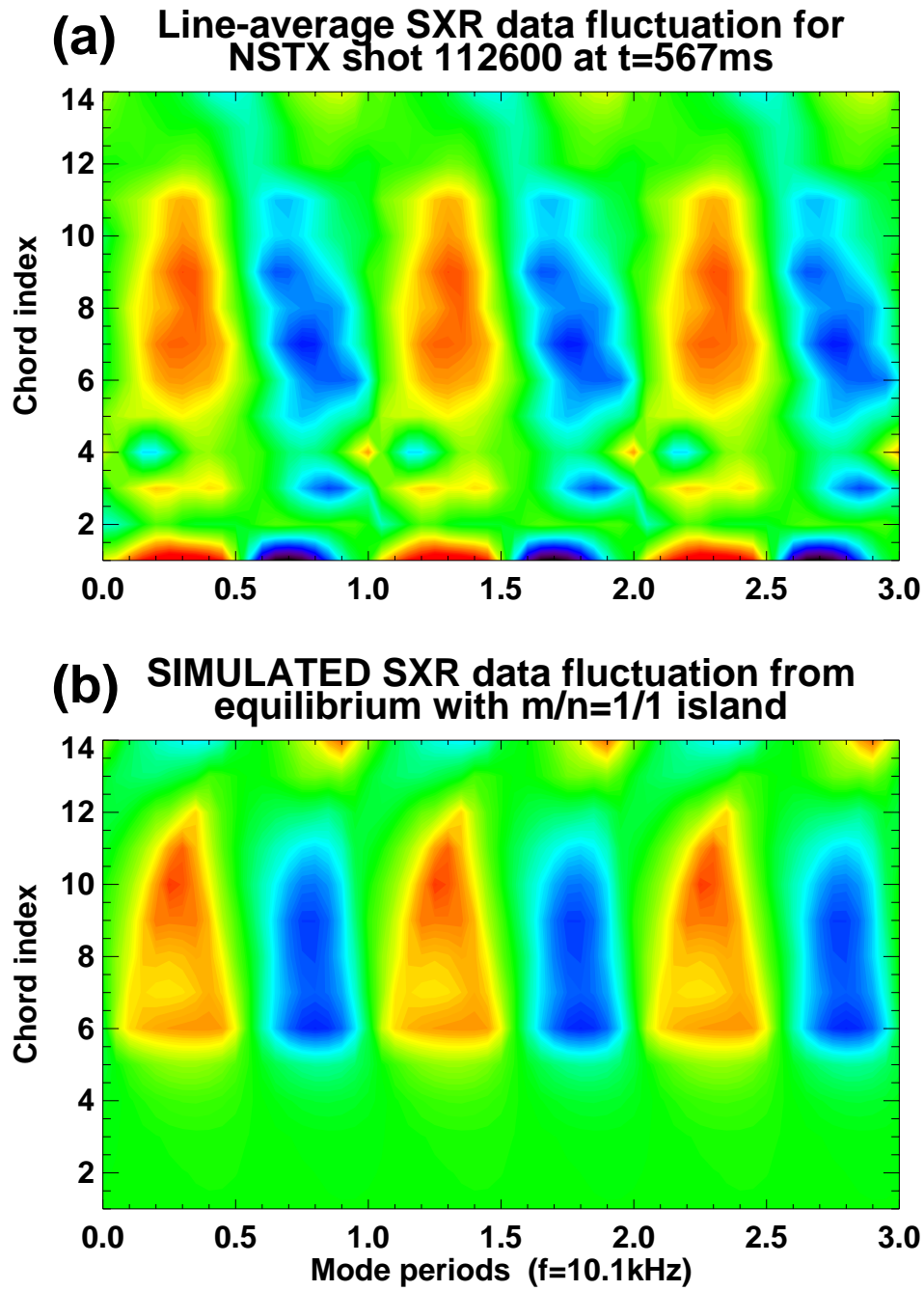
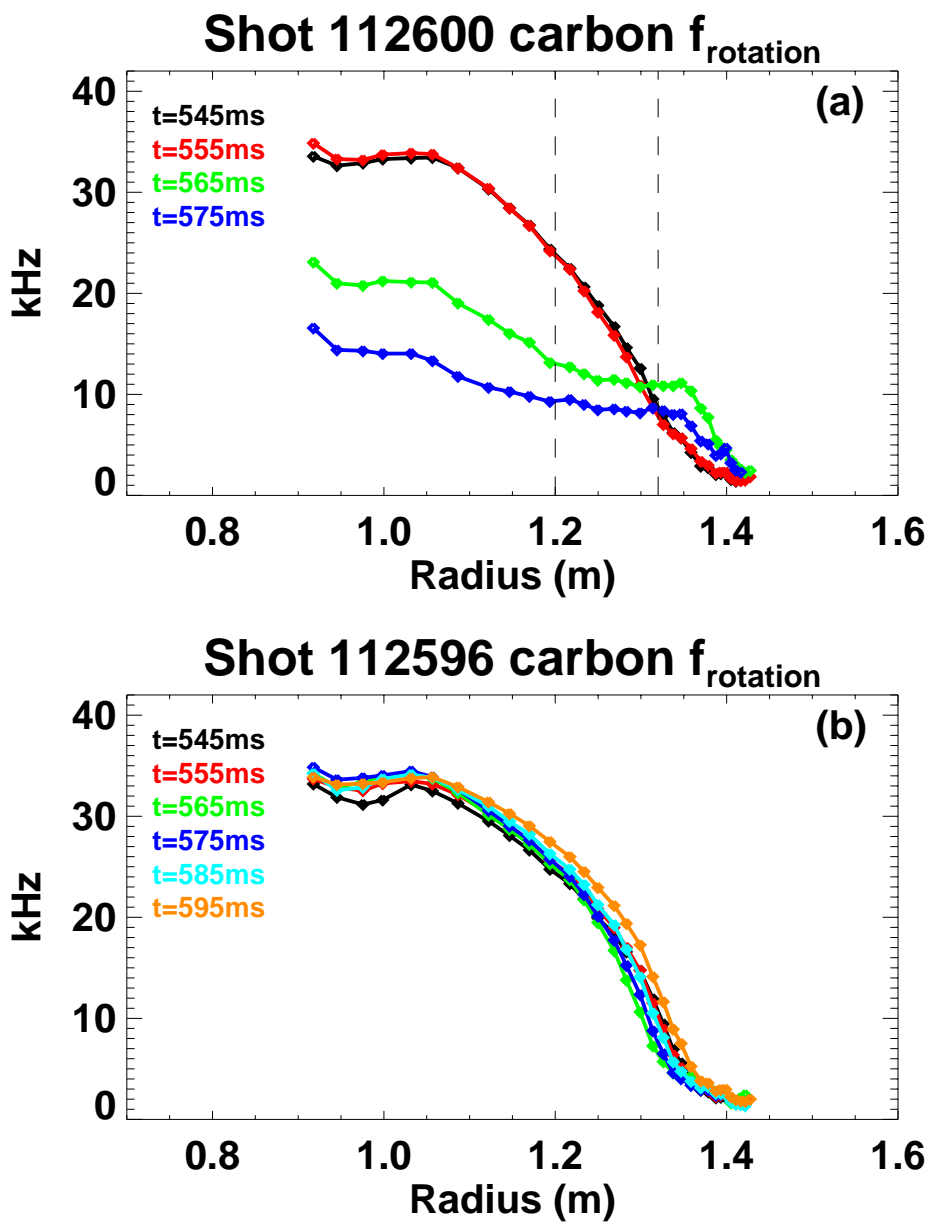


Figure 13. Mode evolution leading to the final disruption of high- $\beta$  discharge 112600.



**Figure 14.** (a) Contours of USXR line-average emission fluctuation in time versus chord index for shot 112600 at  $t=567\text{ms}$ , and (b) best-fit to the emission data using the single-helicity island model with  $m/n = 1/1$ .



**Figure 15.** Rotation profile evolution for discharges (a) 112600 and (b) 112596 from Figure 10.

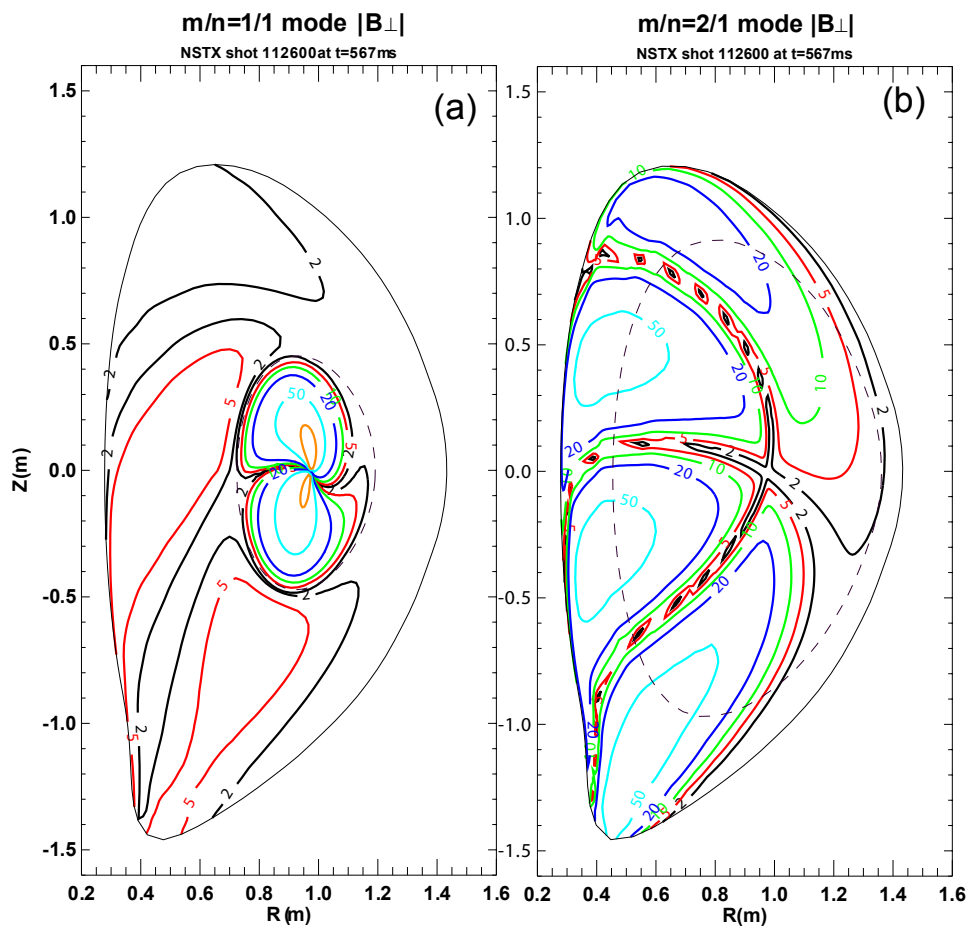


**Figure 16.** Magnitude of the flux-surface-normal component of the perturbed magnetic field for the (a) 1/1 mode and (b) 2/1 mode using separate single helicity island model fits to the core and off-axis mode data shown in Figure 14.

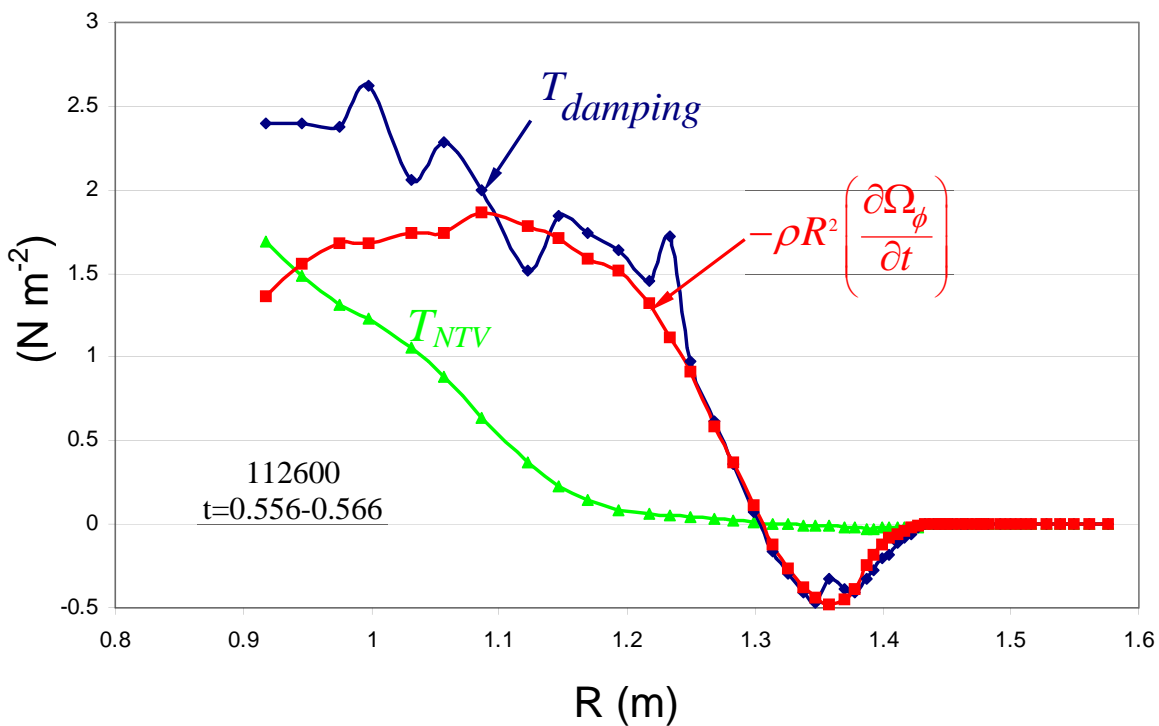


**Figure 17.** Measured rotation damping profile during the early growth phase of the 1/1 mode in shot 112600 compared to the predicted damping from NTV theory using the island fields from Figure 16.



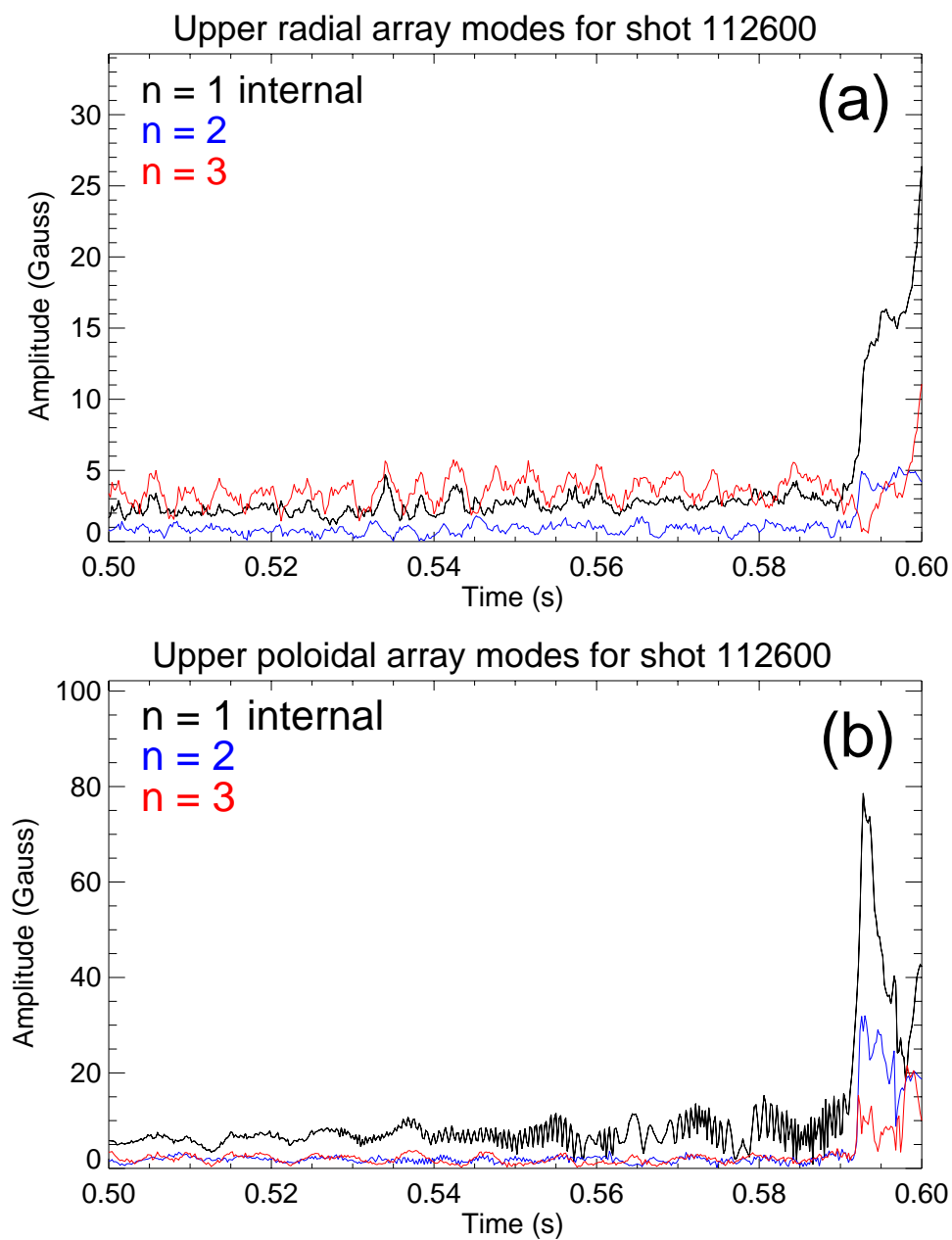


**Figure 18.** Decomposition of in-vessel magnetic field fluctuations into  $n=1-3$  components for (a) upper radial and (b) upper poloidal sensors before and during the rotation damping phase of shot 112600.

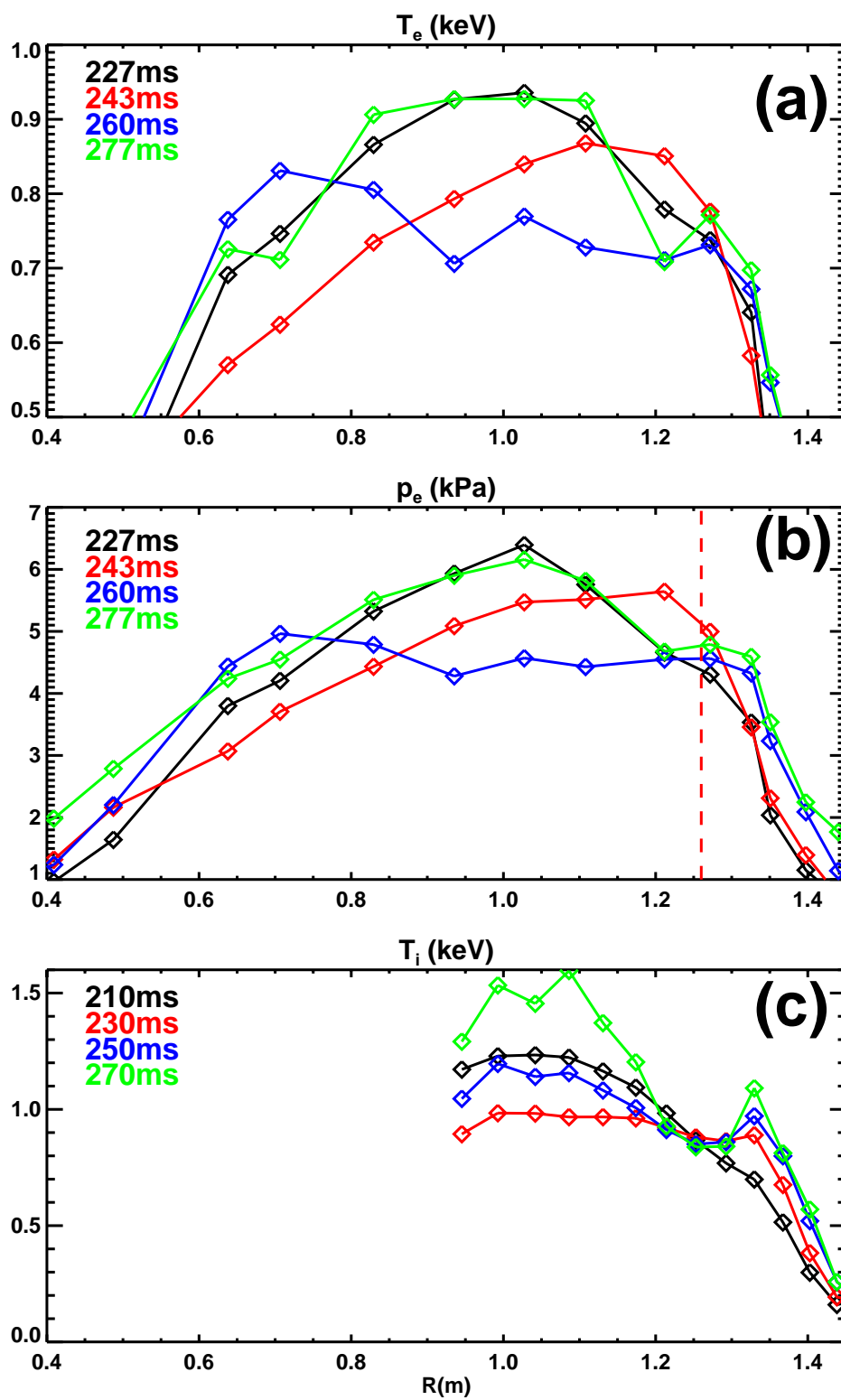


**Figure 19.** Thomson scattering (a) electron temperature, (b) electron pressure, and (c) 20ms time-averaged ion temperature from CHERS before and during the 1/1 mode activity in shot 108103.

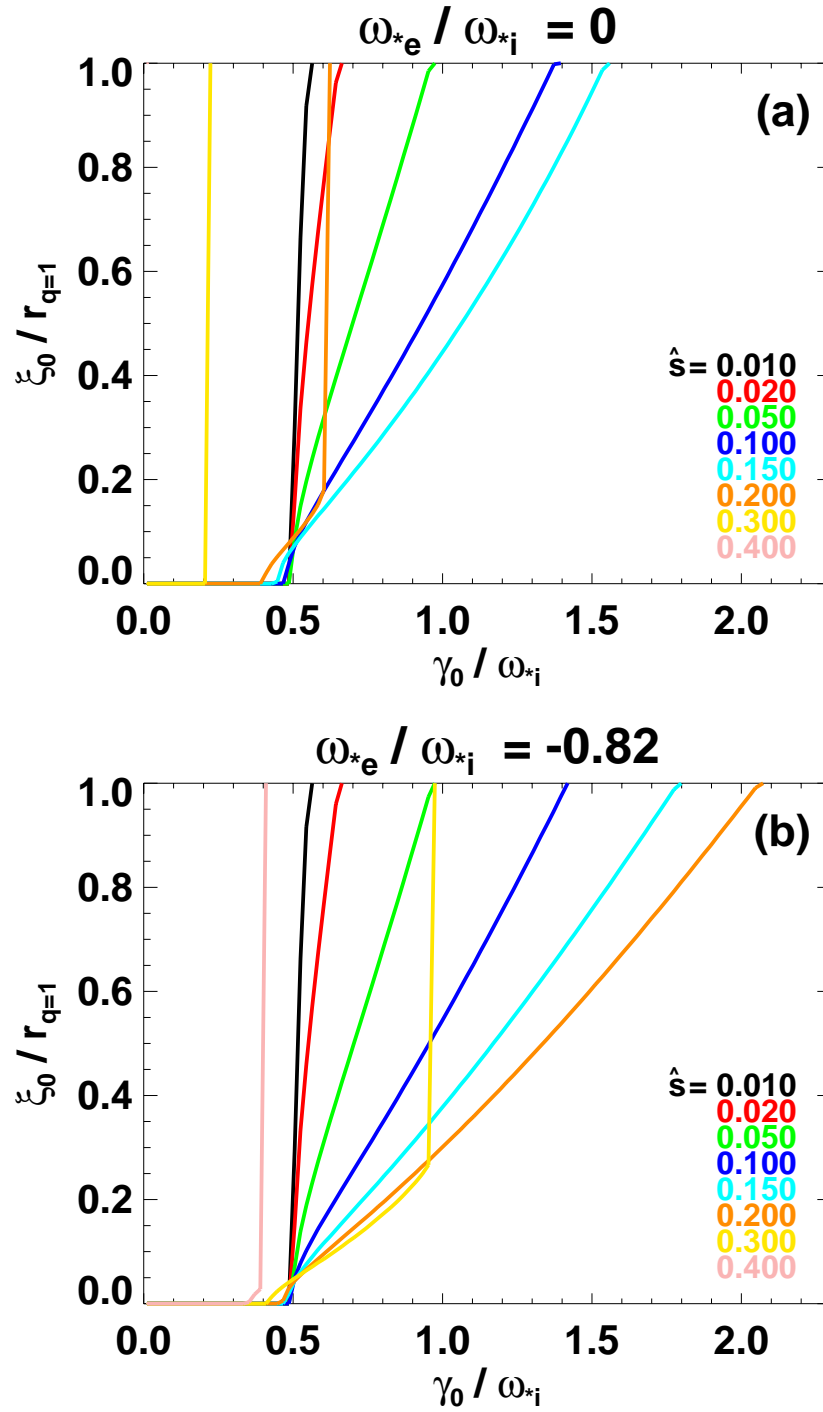


**Figure 20.** Predicted displacement of the plasma core (normalized to the radius of the  $q=1$  surface) during non-linear 1/1 mode saturation in the Rogers-Zakharov model (a) ignoring the electron diamagnetic drift, and (b) including the electron diamagnetic drift for shot 108103 at  $t=220$ ms.

## External Distribution

Plasma Research Laboratory, Australian National University, Australia  
Professor I.R. Jones, Flinders University, Australia  
Professor João Canalle, Instituto de Fisica DEQ/IF - UERJ, Brazil  
Mr. Gerson O. Ludwig, Instituto Nacional de Pesquisas, Brazil  
Dr. P.H. Sakanaka, Instituto Fisica, Brazil  
The Librarian, Culham Laboratory, England  
Mrs. S.A. Hutchinson, JET Library, England  
Professor M.N. Bussac, Ecole Polytechnique, France  
Librarian, Max-Planck-Institut für Plasmaphysik, Germany  
Jolan Moldvai, Reports Library, Hungarian Academy of Sciences, Central Research Institute  
for Physics, Hungary  
Dr. P. Kaw, Institute for Plasma Research, India  
Ms. P.J. Pathak, Librarian, Institute for Plasma Research, India  
Ms. Clelia De Palo, Associazione EURATOM-ENEA, Italy  
Dr. G. Grosso, Instituto di Fisica del Plasma, Italy  
Librarian, Naka Fusion Research Establishment, JAERI, Japan  
Library, Laboratory for Complex Energy Processes, Institute for Advanced Study,  
Kyoto University, Japan  
Research Information Center, National Institute for Fusion Science, Japan  
Dr. O. Mitarai, Kyushu Tokai University, Japan  
Dr. Jiengang Li, Institute of Plasma Physics, Chinese Academy of Sciences,  
People's Republic of China  
Professor Yuping Huo, School of Physical Science and Technology, People's Republic of China  
Library, Academia Sinica, Institute of Plasma Physics, People's Republic of China  
Librarian, Institute of Physics, Chinese Academy of Sciences, People's Republic of China  
Dr. S. Mirnov, TRINITI, Troitsk, Russian Federation, Russia  
Dr. V.S. Strelkov, Kurchatov Institute, Russian Federation, Russia  
Professor Peter Lukac, Katedra Fyziky Plazmy MFF UK, Mlynska dolina F-2,  
Komenskeho Univerzita, SK-842 15 Bratislava, Slovakia  
Dr. G.S. Lee, Korea Basic Science Institute, South Korea  
Institute for Plasma Research, University of Maryland, USA  
Librarian, Fusion Energy Division, Oak Ridge National Laboratory, USA  
Librarian, Institute of Fusion Studies, University of Texas, USA  
Librarian, Magnetic Fusion Program, Lawrence Livermore National Laboratory, USA  
Library, General Atomics, USA  
Plasma Physics Group, Fusion Energy Research Program, University of California  
at San Diego, USA  
Plasma Physics Library, Columbia University, USA  
Alkesh Punjabi, Center for Fusion Research and Training, Hampton University, USA  
Dr. W.M. Stacey, Fusion Research Center, Georgia Institute of Technology, USA  
Dr. John Willis, U.S. Department of Energy, Office of Fusion Energy Sciences, USA  
Mr. Paul H. Wright, Indianapolis, Indiana, USA

The Princeton Plasma Physics Laboratory is operated  
by Princeton University under contract  
with the U.S. Department of Energy.

Information Services  
Princeton Plasma Physics Laboratory  
P.O. Box 451  
Princeton, NJ 08543

Phone: 609-243-2750  
Fax: 609-243-2751  
e-mail: [pppl\\_info@pppl.gov](mailto:pppl_info@pppl.gov)  
Internet Address: <http://www.pppl.gov>